The Astrophysical Journal, 623:742–762, 2005 April 20

THE BOLOCAM LOCKMAN HOLE MILLIMETER-WAVE GALAXY SURVEY: GALAXY CANDIDATES AND NUMBER COUNTS

G. T. Laurent,[1] J. E. Aguirre,[1] J. Glenn,[1] P. A. R. Ade,[2] J. J. Bock,[3,4] S. F. Edgington,[4] A. Goldin,[3] S. R. Golwala,[4] D. Haig,[2] A. E. Lange,[4] P. R. Maloney,[1] P. D. Mauskopf,[2] H. Nguyen,[3] P. Rossinot,[4] J. Sayers,[4] and P. Stover[1]

Received 2004 August 27; accepted 2005 January 11

ABSTRACT

We present results of a new deep 1.1 mm survey using Bolocam, a millimeter-wavelength bolometer array camera designed for mapping large fields at fast scan rates, without chopping. A map, galaxy candidate list, and derived number counts are presented. This survey encompasses 324 arcmin^2 to an rms noise level (filtered for point sources) of $\sigma_{1.1\,\mathrm{mm}} \simeq 1.4$ mJy beam^{-1} and includes the entire regions surveyed by the published 8 mJy 850 μm JCMT SCUBA and 1.2 mm IRAM MAMBO surveys. We reduced the data using a custom software pipeline to remove correlated sky and instrument noise via a principal component analysis. Extensive simulations and jackknife tests were performed to confirm the robustness of our source candidates and estimate the effects of false detections, bias, and completeness. In total, 17 source candidates were detected at a significance ≥ 3.0 σ, with six expected false detections. Nine candidates are new detections, while eight candidates have coincident SCUBA 850 μm and/or MAMBO 1.2 mm detections. From our observed number counts, we estimate the underlying differential number count distribution of submillimeter galaxies and find it to be in general agreement with previous surveys. Modeling the spectral energy distributions of these submillimeter galaxies after observations of dusty nearby galaxies suggests extreme luminosities of $L = (1.0\text{–}1.6) \times 10^{13}\ L_\odot$ and, if powered by star formation, star formation rates of 500–800 $M_\odot$ yr^{-1}.

Subject headings: galaxies: high-redshift — galaxies: starburst — submillimeter

1. INTRODUCTION

Submillimeter galaxies are extremely luminous ($L > 10^{12}\ L_\odot$), high-redshift ($z > 1$), dust-obscured galaxies detected by their thermal dust emission (for a review see Blain et al. 2002). The dust is heated by the ultraviolet and optical flux from young stars associated with prodigious inferred star formation rates (SFRs) of $\sim$100–1000 $M_\odot$ yr^{-1} (Blain et al. 2002). Although $\sim\frac{1}{3}$ of sources appear to contain an active galactic nucleus (AGN; Alexander et al. 2003; Ivison et al. 2004), in nearly all cases the AGNs are not bolometrically important (<20%; Alexander et al. 2004). Given these SFRs, a burst of duration 10^8 yr would be sufficient to form all the stars in an elliptical galaxy, making it plausible that submillimeter galaxies are the progenitors of elliptical galaxies and spiral bulges (Smail et al. 2002; Swinbank et al. 2004). Deep (sub)millimeter surveys with SCUBA (Holland et al. 1999) and MAMBO (Bertoldi et al. 2000) have now resolved 10%–40% of the cosmic far-infrared background (Puget et al. 1996; Hauser et al. 1998; Fixsen et al. 1998) into submillimeter galaxies in blank-field surveys (e.g., Greve et al. 2004; Borys et al. 2003; Scott et al. 2002) and 40%–100% using lensing galaxy clusters (Blain et al. 1999; Cowie et al. 2002). Photometric redshifts constrain most of the submillimeter galaxies found so far to lie at $z > 1$ (e.g., Carilli & Yun 1999; Yun & Carilli 2002; Aretxaga et al. 2003).

Recent observations of submillimeter galaxies with the Keck Low-Resolution Imaging Spectrograph (LRIS; Chapman et al. 2003a, 2003b, 2005) have shown that redshifts can be obtained for $\sim$70% of bright submillimeter galaxies ($S_{850\,\mu\mathrm{m}} > 5$ mJy) with bright radio counterparts ($S_{1.4\,\mathrm{GHz}} > 30$ μJy; Blain et al. 2004) (the fraction of submillimeter galaxies with radio counterparts appears to be $\sim$65%; Ivison et al. 2002). This sample of submillimeter galaxies lies in a distribution peaking at $z = 2.4$ with $\Delta z = 0.65$ (Ivison et al. 2002; Chapman et al. 2003b, 2005). Six of these galaxies have had their optical spectroscopic redshifts confirmed by millimeter CO line measurements (Frayer et al. 1998, 1999; Neri et al. 2003; Sheth et al. 2004). This redshift distribution may be biased with respect to the overall submillimeter galaxy population owing to a number of selection effects: the requirement of precise radio positions prior to spectroscopy, which introduces a bias against cooler galaxies, especially at higher redshifts ($z > 2.5$); limited completeness ($\sim$30%) of the spectroscopic observations, which biases the sample against galaxies with weak emission lines; and the redshift gap at $z = 1.2\text{–}1.8$ due to the "spectroscopic desert," in which no strong rest-frame ultraviolet lines are redshifted into the optical.

Bolocam is a new millimeter-wave bolometer camera for the Caltech Submillimeter Observatory (CSO).[5] Bolocam's large field of view (8′), 31″ beams (FWHM at $\lambda = 1.1$ mm), and AC biasing scheme make it particularly well suited to finding rare, bright submillimeter galaxies and for probing large-scale structure. We have used Bolocam to conduct a survey toward the Lockman Hole for submillimeter galaxies. The Lockman Hole is a region in UMa in which absorbing material, such

[1] Center for Astrophysics and Space Astronomy and Department of Astrophysical and Planetary Sciences, University of Colorado, 593 UCB, Boulder, CO 80309-0593; glaurent@colorado.edu.

[2] Physics and Astronomy, Cardiff University, 5, The Parade, P.O. Box 913, Cardiff, CF24 3YB Wales, UK.

[3] Jet Propulsion Laboratory, California Institute of Technology, 4800 Oak Grove Drive, Pasadena, CA 91109.

[4] California Institute of Technology, 1200 East California Boulevard, MC 59-33, Pasadena, CA 91125.

[5] See http://www.cso.caltech.edu/bolocam.

as dust and galactic hydrogen, is highly rarefied (H I column density of $N_{\rm H} \approx 4.5 \times 10^{19}$ cm^{-2}; Jahoda et al. 1990), providing a transparent window for sensitive extragalactic surveys over a wide spectral range, from the infrared and millimeter wavebands to UV and X-ray observations. Submillimeter (Scott et al. 2002; Fox et al. 2002; Ivison et al. 2002; Eales et al. 2003) and millimeter-wave (Greve et al. 2004) surveys for submillimeter galaxies have already been done toward the Lockman Hole. It is one of the one-quarter square degree fields of the SCUBA SHADES,[6] the focus of a deep extragalactic survey with *XMM-Newton* (Hasinger et al. 2001), and a target field for *Spitzer* guaranteed time observations. The coverage of the Lockman Hole region by several surveys therefore makes it an excellent field for intercomparison of galaxy candidate lists and measuring spectral energy distributions (SEDs), which will ultimately enable dust temperatures and redshifts to be constrained.

This paper is arranged as follows. In § 2 Bolocam and the observations are described. In § 3 the data reduction pipeline, including pointing and flux calibration, cleaning and sky subtraction, and mapping, is described. In § 4 the source candidate list and tests of the robustness of the candidates are presented. We devote § 5 to the extraction of the number counts versus flux density relation using simulations designed to characterize the systematic effects in the data reduction and the false detections, completeness, and bias in the survey. In § 6 we discuss the implications of the survey, in § 7 we describe future work for this program, and in § 8 we give conclusions.

2. OBSERVATIONS

2.1. *Instrument Description*

The heart of Bolocam is an array of 144 silicon nitride micromesh ("spiderweb") bolometers cooled to 260 mK by a three-stage (^{4}He/^{3}He/^{3}He) sorption refrigerator. An array of close-packed ($1.5f\lambda$), straight-walled conical feed horns terminating in cylindrical waveguides and integrating cavities formed by a planar backshort couples the bolometers to cryogenic and room-temperature optics. The illumination on the 10.4 m diameter CSO primary mirror is controlled by the combination of the feed horns and a cold (6 K) Lyot stop, resulting in 31″ beams (FWHM). A stack of resonant metal-mesh filters form the passband in conjunction with the waveguides. A $\lambda = 2.1$ mm configuration is also available, which is used for observations of the Sunyaev-Zel'dovich effect and secondary anisotropies in the cosmic microwave background radiation. Technical details of Bolocam are given in Glenn et al. (1998, 2003) and Haig et al. (2004); numerical simulations of the integrating cavities are described in Glenn et al. (2002).

A key element of Bolocam is the bolometer bias and readout electronics: an AC biasing scheme (130 Hz) with readout by lock-in amplifiers enables the detectors to be biased well above the $1/f$ knee of the electronics. The electronic readout stability, in conjunction with Bolocam's rigorous sky noise subtraction algorithm, eliminates the need to nutate the CSO subreflector. Another advantage of this AC biasing scheme is that it is easy to monitor the bolometer operating voltage; these voltages are determined by the total atmospheric emission in the telescope beam and the responsivity of the bolometers. Thus, a voltage that is a monotonic function of the in-band atmospheric optical depth and bolometer responsivity is continually measured. Sky subtraction is implemented by either a subtraction of the average bolometer voltages or a principal component analysis (PCA) technique, which is described below.

[6] See http://www.roe.ac.uk/ifa/shades/links.html.

2.2. *Scan Strategy*

Two sets of observations of the Lockman Hole East (R.A. = $10^{\rm h}52^{\rm m}08\overset{\rm s}{.}82$, decl. = $+57^\circ21'33\overset{''}{.}80$, J2000.0) were made with Bolocam: 2003 January, when the data were taken with a fast raster scan without chopping (hereafter referred to as raster scan observations), and 2003 May, when the data were acquired with a slow raster scan with chopping as a test of this observing mode (referred to as chopped observations). Approximately 82 hr of integration time over 17 nights were obtained on the field during 2003 January, resulting in 259 separate observations, and 41 hr over 19 nights were obtained in 2003 May, resulting in 64 separate observations. The weather was generally good during the 2003 January run and mediocre to poor during the 2003 May run, where we characterize the weather quality by the sky noise variability (rapid variability of the optical depth).[7] One hundred and nineteen bolometer channels were operational during 2003 May; however, only 89 bolometer channels were used in the analysis of the 2003 January data. (The remaining bolometers were not included in making the final Lockman Hole map because of excess noise and/or electronics failures.) Nominally one feed horn per hextant is blocked to enable these dark bolometers to be used for bias and noise monitoring. The 2003 May chopped observations were not deep enough to detect galaxies individually at >3 σ and were used only for pointing verification by cross-correlation with the raster scan observations.

During 2003 January, observations were made by scanning the telescope at 60″ s^{-1} in right ascension and stepping in declination by 162″ ($\sim\frac{1}{3}$ of a field of view) between subscans (defined as a single raster scan across the sky at a fixed declination) to build up the map. Subsequent scans (which we define as the set of subscans needed to cover the entire declination range of the field) were taken with a $\pm 11''$ jitter for each 162″ step to minimize coverage variations. Combined with a 5° tilt of the bolometer array relative to azimuth and a fixed Dewar angle, such that the rotation relative to scan direction varies over the night, this yielded even coverage and sub-Nyquist sampling in the cross scan direction (declination). Sub-Nyquist sampling was automatically achieved in the in-scan direction (right ascension) with 50 Hz sampling of the lock-in amplifiers. In 2003 May, the chopped observations were made with raster scans in azimuth and steps in elevation, but with a scan rate of 5″ s^{-1} and a symmetric chopper throw of $\pm 45''$ in azimuth, with frequencies of 1 and 2 Hz.

A coverage map of the Bolocam Lockman Hole East field from 2003 January is shown in Figure 1, where the integration time per $10'' \times 10''$ pixel is shown. Bolocam's 8′ field of view is not small compared to the map size; thus, there is a large border around the map where the coverage is reduced and nonuniform compared to the central region. Hence, we define a "uniform coverage region" of 324 arcmin^2 in the center where the rms in the integration time per pixel is 12%. Because rms noise varies as the square root of the integration time, the noise dispersion is approximately 6% in the uniform coverage region (2% after the

[7] Another weather measurement influencing the Bolocam mapping speed is the CSO 225 GHz heterodyne, narrowband, "tipper tau" monitor, which measures the zenith atmospheric attenuation. The 2003 January and May Lockman Hole observations yielded $\tau_{225\ \rm GHz}$ ranges and 75th percentiles of $\tau_{225\ \rm GHz} = 0.028$–$0.129$, $\tau_{75\%} = 0.083$ and $\tau_{225\ \rm GHz} = 0.014$–$0.307$, $\tau_{75\%} = 0.200$, respectively.

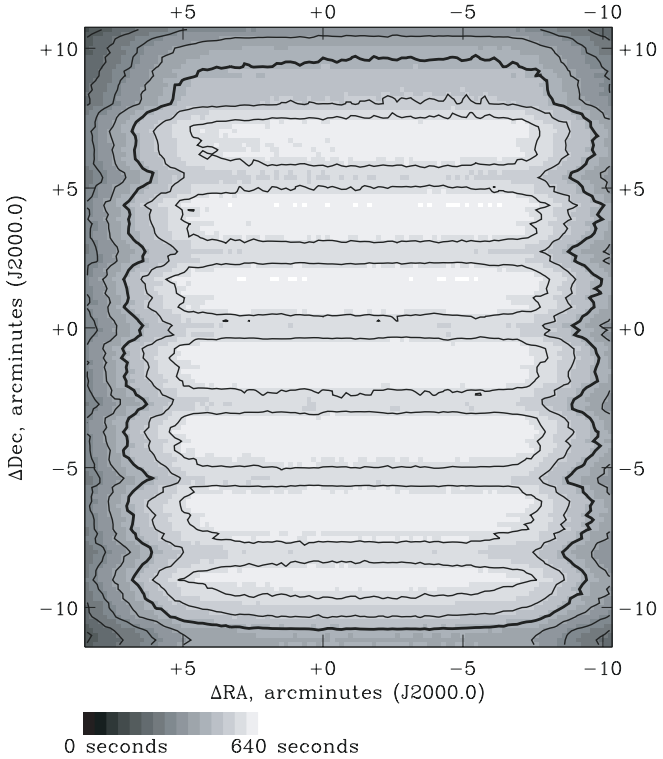

FIG. 1.—Coverage map of the Lockman Hole East, pixelized at 10″ resolution. White corresponds to the highest level of coverage and black to the lowest level of coverage; the contours are 193, 257, 322, 386, 450, 515, and 579 s of integration time per pixel. The "uniform coverage region" corresponds to the thick contour at 450 s pixel^{-1}.

map has been optimally filtered as discussed in § 3.5). Our analysis is confined to the uniform coverage region. The observational parameters are summarized in Table 1.

3. DATA REDUCTION

3.1. *Basic Pipeline*

The Lockman Hole observations were reduced with a custom IDL-based software pipeline. The raw files were cleaned with a PCA sky subtraction, where an atmospheric and instrumental noise template was generated through an eigenvector decomposition of the time stream data (§ 3.2). In the case of the chopped observations, which are characterized by both positive and negative beams, the time streams were first demodulated followed by a convolution with the expected source crossing structure (first the positive beam, then the negative beam). This results in a positive net peak at the nominal source position with the full source amplitude and symmetric negative beams with half the source amplitude.

Once the cleaned time streams were obtained, a map was generated by co-adding individual time streams, weighted by their power spectral densities (PSDs) integrated over the spectral response to a point source. Pointing offsets were applied to individual observations from the global pointing model generated from observations of submillimeter pointing sources (§ 3.3). Time streams were calibrated from lock-in amplifier voltages to millijanskys using observations of primary and secondary flux calibrators (§ 3.4). The final map was generated in right ascension and declination using sub–beam-sized pixelization (§ 3.5) and Wiener filtered to maximize signal-to-noise ratio (S/N) for detections of point sources.

TABLE 1
OBSERVATIONAL PARAMETERS

Quantity	Value
Field of view (arcmin)	8
Beam size (FWHM) (arcsec)	31
1.1 mm band center (GHz)	265
Bandwidth (GHz)	42
Raster scan speed[a] (arcsec s^{-1})	60
Chopped observation scan speed[b] (arcsec s^{-1})	5
Chopper throw[c] (arcsec)	90
Subscan step size (arcsec)	162
Subscan substep size (arcsec)	±11

[a] Raster scans were scanned in right ascension with steps between subscans in declination.
[b] Chopped observations were scanned in azimuth with steps between subscans in elevation.
[c] For chopped observations only.

3.2. *Cleaning and Sky Subtraction*

To facilitate removal of fluctuating atmospheric water vapor emission (sky noise) from the bolometer signals, Bolocam was designed such that the feed horn beams overlap maximally on the primary mirror of the telescope and therefore sample very similar columns of atmosphere. Thus, the sky noise, which dominates the fundamental instrument noise by a factor of ∼100, is a nearly common-mode signal. To remove this correlated $1/f$ noise with maximum effectiveness, a PCA technique was developed. The formalism of the PCA analysis is standard (see, e.g., Murtagh & Heck 1987). Here the covariance matrix is built from the n bolometers by m time elements matrix for each subscan. Eigenfunctions of the orthogonal decomposition that have "large" eigenvalues, corresponding to large contributions to the correlated noise, are nulled and the resulting functions are transformed back into individual bolometer time streams. This technique is applicable for the dim ($\lesssim$10 mJy) submillimeter galaxies of the Lockman Hole (and other blank-field surveys) because the source signal contributes negligibly to the sky templates and is largely uncorrelated from bolometer to bolometer. The PCA technique is not appropriate for extended sources, however, in which case the bolometers see correlated astrophysical signals, which are then attenuated. The PCA decomposition was applied to raster scan and chopped data, after chop demodulation in the latter case. Cosmic-ray strikes (spikes in the time streams) are flagged and not included in constructing the eigenfunctions.

The precise level of the cut on the large eigenvalues is somewhat arbitrary. The greater the number of eigenfunctions that are nulled, the lower the resulting noise in the cleaned time stream, but the correspondingly greater source flux density removed. Empirically, an iterative cut with the nulling of eigenfunctions with eigenvalues >3 σ from the mean of the eigenvalue distribution produced a balance between sky emission removal and source flux density reduction in simulated observations by maximizing the S/N. Because the distribution of eigenvalues for each observation is characterized by a few outliers (typically 4–7) at large σ-values, the overall variance of the time stream is largely dominated by these eigenvalues, resulting in an S/N that is insensitive to the cut threshold for 2–5 σ. Furthermore, the distribution of source candidates in the combined Lockman Hole map was invariant under variations in the cut threshold in this range.

The PCA sky subtraction attenuates the signal from point sources in addition to the atmospheric signal because it removes

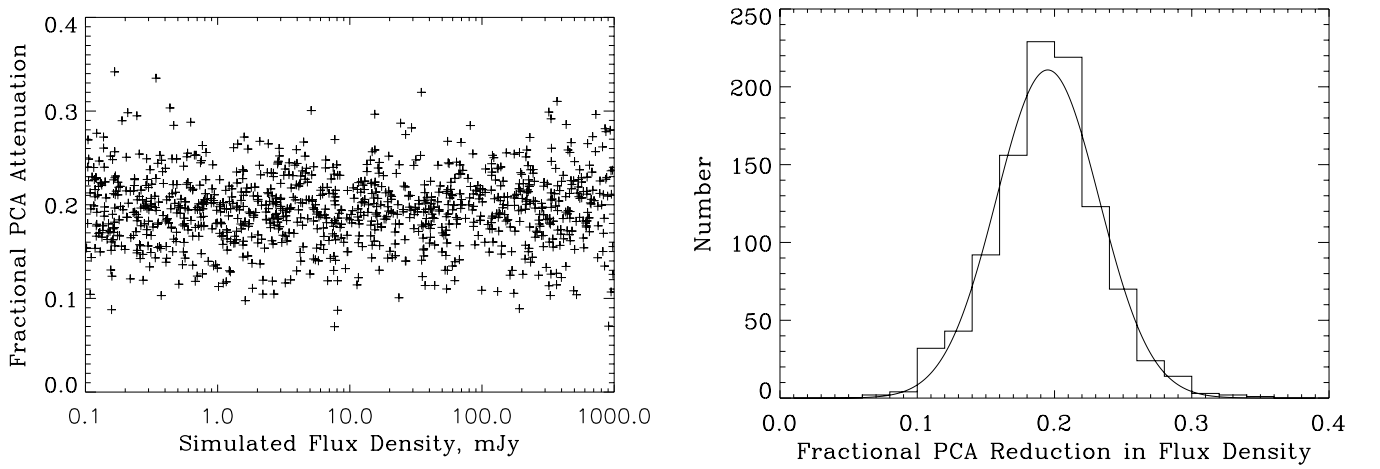

FIG. 2.—Source attenuation by PCA cleaning as a function of injected flux density (*left*) and histogram with Gaussian fit (*right*). Sources were injected into the raw time streams, which were then cleaned using the PCA. The resulting source amplitudes were compared to the injected source amplitudes (their ratio is the fractional reduction in source flux density). The attenuation of sources by PCA is 19% with a dispersion of 4%, independent of flux density from 0.1 mJy to 1 Jy.

low-frequency power from the time streams. The amount of flux density attenuation is determined by the number of PCA components that are removed from the raw time streams, which is controlled by the cut on the eigenvalues: a more aggressive cut results in greater attenuation. Monte Carlo simulations were done to determine the amount by which the flux density of galaxy candidates was reduced by the cleaning. The simulations were done in the following manner: A fake source (Gaussian, 31″ FWHM) was injected into a blank Lockman Hole map. A simulated bolometer time stream was generated from the map of the fake source and was added to the raw bolometer time streams of an individual Lockman Hole observation. The time stream data were then cleaned with PCA and mapped in the ordinary manner. The resulting source was fitted by a two-dimensional Gaussian to determine the attenuation of the injected source flux density. This simulation was repeated 1014 times with fake sources injected into random observations at random positions and ranging in flux density from 0.1 to above 1000 mJy (Fig. 2). The average reduction in flux density is 0.19 with an rms dispersion of 0.04, independent of flux density to 1 Jy.

Above 1 Jy, typical for bright pointing and flux calibrators, the amount of attenuation by PCA was found to depend on the brightness of the fake source. Thus, a different cleaning technique was used for these sources. An atmospheric noise template was generated by simply taking an average of all n bolometers for each time element. The mean-subtracted sky template was then correlated to each of the individual bolometer time streams and the correlated component was subtracted. To prevent the correlation coefficient from being contaminated by the calibrators, multiple scans (including telescope turnaround time between scans) were concatenated and used together to correlate the average sky template to each individual bolometer signal, thus ensuring a small contribution from the point source. A similar analysis to that for PCA flux reduction was performed for the simple average sky subtraction technique, yielding an average flux density reduction of 0.07, independent of source flux, with an rms dispersion of 0.02.

3.3. *Pointing*

Observations of planets, quasars, protostellar sources, H II regions, and evolved stars were used to construct separate pointing models for the 2003 January and May observing runs. Observations of the pointing sources were taken at the same scanning speeds as the Lockman Hole observations. The pointing fields were generally small (scan areas of $\sim 4' \times 4'$), although several larger maps ($10' \times 10'$) were made of Mars so that the source would pass over the entire bolometer array for measuring relative responsivities and beam maps. Pointing observations are generally small because source crossings are only needed in a small subset (15 or so) of bolometers to determine the pointing offsets. These observations were used to map and correct the distortion over the field of view, which is in broad agreement with the distortion predicted by a Zemax® ray-tracing model. The residual rms in the raster-scanned pointing model for the ensemble of all 2003 January sources is 9.″1, although the local pointing registered to a nearby pointing source is superior.[8] This random pointing error results in an 18% flux density reduction of the Lockman Hole galaxy candidates (analytically derived from a convolution of the 31″ Bolocam beam with a 9.″1 Gaussian random pointing error), which is corrected for in the reported flux densities (and uncertainties in these fluxes) of Table 2.

While the 2003 January pointing observations were used to construct a pointing model that was applied to the entire sky, the region of the celestial sphere near the Lockman Hole was not well sampled. A pointing correction derived from sources far away (>30°) from the Lockman Hole is therefore susceptible to a systematic offset. Pointing observations were made much more frequently (once per hour) during the 2003 May run and sources near the Lockman Hole were emphasized to create an improved local pointing model; consequently, the 2003 May pointing model near the Lockman Hole was superior to the 2003 January pointing model. No galaxy candidates were detected at $\geq 3\ \sigma$ significance in the 2003 May chopped Lockman Hole map owing to poor weather; however, it was cross-correlated with the 2003 January map to compare the pointing models. The cross-correlation yielded a shift of 25″ in right ascension of the 2003 January data with respect to the 2003 May data (Fig. 3). Because the pointing on the sky near the Lockman Hole was substantially better and more frequently sampled for the 2003 May run, we attribute this shift to a systematic offset in the 2003 January pointing model. Thus, a systematic 25″ shift in right

[8] A subsequent pointing model for a localized region of sky yields an rms of 4.″5.

TABLE 2
Galaxy Candidates

Source	R.A. (J2000.0)	Decl. (J2000.0)	S/N	Corrected S_ν	Corrected σ
1.....	10 52 55.5	57 21 03	5.0	6.8	1.4
2.....	10 51 16.7	57 16 33	4.8	6.5	1.4
3.....	10 52 12.2	57 15 53	4.5	6.0	1.4
4.....	10 52 03.6	57 18 23	4.0	5.2	1.4
5.....	10 52 29.5	57 22 03	3.9	5.1	1.3
6.....	10 51 15.6	57 14 23	3.5	5.0	1.5
7.....	10 51 30.0	57 31 03	3.4	4.9	1.5
8.....	10 52 37.0	57 24 33	3.7	4.8	1.3
9.....	10 53 05.2	57 15 23	3.1	4.8	1.5
10.....	10 51 31.4	57 23 13	3.5	4.7	1.4
11.....	10 52 48.0	57 12 43	3.2	4.6	1.5
12.....	10 51 15.5	57 15 23	3.2	4.6	1.4
13.....	10 52 35.7	57 17 53	3.3	4.5	1.4
14.....	10 52 01.1	57 25 03	3.3	4.4	1.3
15.....	10 51 47.4	57 28 33	3.2	4.4	1.4
16.....	10 52 27.1	57 25 13	3.1	4.1	1.4
17.....	10 51 59.9	57 24 23	3.1	4.0	1.3

Note.—Units of right ascension are hours, minutes, and seconds, and units of declination are degrees, arcminutes, and arcseconds.

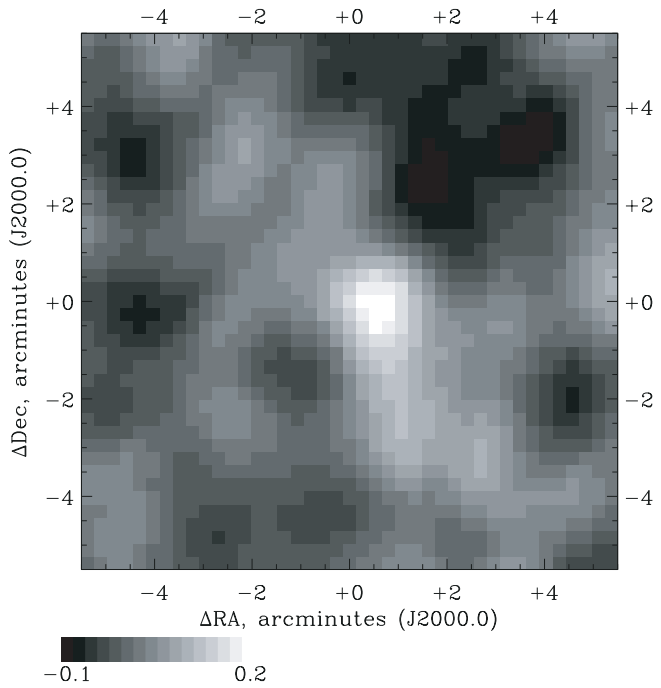

Fig. 3.—Cross-correlation of the 2003 January and May Lockman Hole maps, pixelized at 10″ resolution. While the weather was too poor during the 2003 May observations to yield any >3 σ detections, the local pointing near the Lockman Hole was sampled substantially better than for the 2003 January run. The 25″ pointing offset corresponding to the peak in the cross-correlation map was subsequently applied to the 2003 January data.

ascension was applied to the 2003 January Lockman Hole map. The need for the shift is also apparent in a comparison between the Bolocam map and the 8 mJy SCUBA 850 μm and MAMBO 1.2 mm surveys, as several of the Bolocam galaxy candidates become coincident with SCUBA and MAMBO sources in the overlap region of the surveys.

Because no pointing observations were taken near the Lockman Hole, it is difficult to quantify the uncertainty in the 9.″1 pointing rms. An independent measurement of our pointing uncertainty was performed by examining both 10 VLA[9] radio positions coincident with Bolocam Lockman Hole galaxy candidates and the subset of 5 sources with additional SCUBA and/or MAMBO counterparts (see § 4.3). The rms errors between the Bolocam and radio positions are $10.2^{+3.1}_{-2.4}$ and $9.3^{+4.4}_{-3.0}$ arcsec for the entire 10 source sample and 5 source subset, respectively. The quoted uncertainties are the minimum length 90% confidence intervals for 10 and 5 degrees of freedom (for both $\delta_{\rm R.A.}$ and $\delta_{\rm decl.}$, each of which independently determines the pointing error), respectively.

3.4. *Flux Calibration*

Observations of primary calibrators (planets) and secondary calibrators (protostellar sources, H II regions, and evolved stars) were used for flux calibration. Reference planetary flux densities were obtained from the James Clerk Maxwell Telescope (JCMT) calibration Web site,[10] and flux densities of secondary calibrators were obtained from JCMT calibrators (Sandell 1994; Jenness et al. 2002). The flux density of IRC +10216 is periodic; the flux density was adjusted to the epoch of observation using the 850 μm SCUBA phase. The reference flux densities were corrected for the Bolocam bandpass, which is centered at 265 GHz (the flux densities in the Bolocam band are 5% larger than the those quoted by the JCMT for the SCUBA 1.1 mm band). During 2003 January, Saturn had a semidiameter of 10″; this is not small compared to the 31″ Bolocam beam, so corrections for the angular extent of Saturn were required.

The standard technique for flux calibration is to calibrate a given science observation using the flux calibrator observations taken nearest in time, which were presumably taken at similar atmospheric opacity and air mass. With Bolocam, we are able to use a more sophisticated technique via continuous monitoring of the bolometer operating resistance using the DC level of the lock-in amplifier output signal. The technique uses the following logic. The atmospheric optical loading increases as the atmospheric optical transmission decreases, which may occur because of changes in zenith opacity (i.e., weather) or intentional changes in telescope elevation. The bolometer resistance decreases monotonically as the atmospheric optical loading increases. Simultaneously, the bolometer responsivity decreases monotonically as the bolometer resistance decreases. Thus, the flux calibration (in nV Jy^{-1}, where the voltage drop across the bolometer is proportional to its resistance), which is proportional to the product of atmospheric transmission and bolometer responsivity, is expected to be a monotonic function of the bolometer resistance. This relation is measured empirically, as shown in Figure 4, by plotting the flux calibration (voltage at the bolometer in nV Jy^{-1} of source flux) from each of the ensemble of calibrator observations against the median DC lock-in amplifier voltage measured during the observation. This relation is then combined with the continuously monitored DC lock-in signal to apply the appropriate flux calibration value during science observations. Note that the curve is measured only using sources dim enough to ensure linear bolometer response; Jupiter was dropped for this reason.

The flux density calibration derived from Figure 4 is biased relative to the blank-field sources by the combination of three effects: reduction in the flux density of calibration sources due

[9] The National Radio Astronomy Observatory is a facility of the National Science Foundation operated under cooperative agreement by Associated Universities, Inc.

[10] See http://www.jach.hawaii.edu/jac-bin/planetflux.pl.

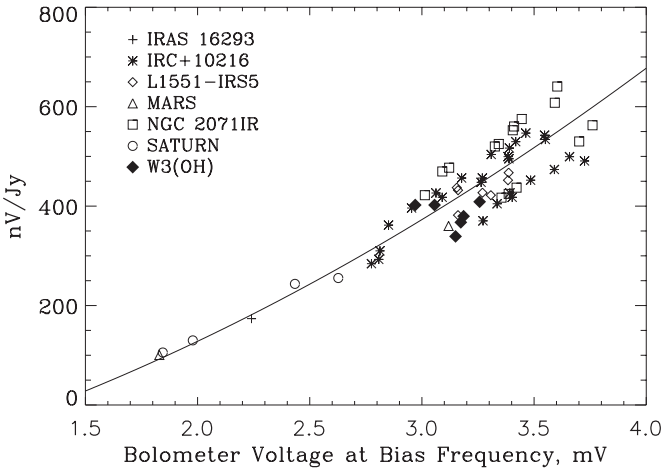

FIG. 4.—Calibration in nV Jy^{-1} (nV at the bolometer) as a function of the demodulated lock-in voltage at the AC bias frequency, which is approximately inversely proportional to the bolometer loading. The quadratic fit is a minimization of the fractional error between observed and expected flux densities. The rms of the residual dispersion in flux density is 9.7%.

to average cleaning, reduction in the flux density of blank-field sources due to PCA cleaning, and reduction in the flux density of blank-field sources due to pointing errors. The first two effects cause the calibration curve of Figure 4 to be shifted up by the factor $\epsilon_{\rm avg}/\epsilon_{\rm PCA}$, where the flux reduction factors $\epsilon_{\rm avg}$ and $\epsilon_{\rm PCA}$ are as determined in § 3.2. The effect of Gaussian random pointing errors of rms σ_p on the peak flux density of a source observed with a Gaussian beam of width σ_b is equivalent to a convolution of the beam with a Gaussian of rms σ_p. The resulting reduction in peak height can be analytically calculated as

$$\epsilon_p = \frac{\sigma_b}{\sqrt{\sigma_b^2 + \sigma_p^2}} = 0.82^{+0.09}_{-0.12}$$

for a 31″ FWHM beam and a random pointing error of 9.″1. The uncertainty quoted for ϵ_p is the minimum length 90% confidence interval obtained from the rms pointing error between the Bolocam galaxy candidates and coincident radio sources (see § 4.3). (While the local pointing observations around a specific altitude and azimuth are clustered, each with a smaller pointing error rms, the Lockman Hole observations were taken over a large range of zenith and azimuthal angles and thus have an overall pointing error defined by the ensemble of pointing observations.)

Thus, the final bias in flux density is

$$\epsilon = \frac{\epsilon_p \epsilon_{\rm PCA}}{\epsilon_{\rm avg}} = 0.71^{+0.08}_{-0.10}.$$

All flux densities (as well as uncertainties in these fluxes) quoted in this paper, including the simulations of § 5, have been corrected for this flux bias. The uncertainty in the flux bias is a systematic effect that produces a correlated shift in all source fluxes.

3.5. *Mapping and Optimal Filtering*

Bolocam maps are built up by co-adding subscans weighted by their time stream PSDs integrated over the spectral (temporal frequency) band of a point source at the raster scan speed. Data points were binned into $10'' \times 10''$ pixels, with approximately 30,000 hits per pixel. Each hit represents a 20 ms integration per bolometer channel. Four maps were created: a coverage map with the number of hits per pixel (Fig. 1); the PCA-cleaned, optimally filtered astrophysical map; a coverage-normalized map; and a within-pixel rms map. In the coverage-normalized map, each pixel was multiplied by the square root of the number of hits (effectively the integration time) in that pixel to account for the nonuniform coverage in the map when comparing pixels. The dispersion of the bolometer voltages (from each of the hits) within each pixel was recorded in the within-pixel rms map.

Because the signal band of interest (point sources) does not fall throughout the entire temporal (or spatial) frequency range of the PSD of the data, we filter the co-added map with an optimal (Wiener) filter, $g(q)$, to attenuate $1/f$ noise at low frequencies and high-frequency noise above the signal frequency:

$$g(q) = \frac{s^*(q)/J(q)}{\int |s(q)|^2/J(q) d^2q}, \quad (1)$$

where $J(q)$ is the average PSD, $s(q)$ is the Fourier transform of the Bolocam beam shape from map space to spatial frequency ($1/x$) space, q, and the asterisk indicates complex conjugation. The factor in the denominator is the appropriate normalization factor so that when convolved with a map, peak heights of beam-shaped sources are preserved. $J(q)$ is obtained by transforming the time stream PSDs (averaged over all of the Lockman Hole observations) to a spatial PSD assuming azimuthal symmetry. A two-dimensional map of equation (1) was thus convolved with the co-added map to maximize S/N for detections of point sources. An analogous filter was applied directly to the demodulated time streams of the chopped observations, with $s(t)$ represented by a positive and negative beam separated by the chop throw (90″).

The cleaned, co-added, optimally filtered map is presented in Figure 5. There is a perimeter a few arcminutes wide around the map that does not lie within the uniform coverage region (cf. Fig. 1). There are 17 galaxy candidates at >3 σ, apparent as unresolved bright spots, numbered in order of decreasing brightness. Six false detections are expected from simulations (discussed in detail in § 5). There are no negative sidelobes associated with the source candidates because the observations are not chopped. The 850 μm SCUBA 8 mJy (Scott et al. 2002) and 1.2 mm MAMBO (Greve et al. 2004) surveys cover patches with radii of $\sim 5'$ and $\sim 7'$ in the center of the map (central 122 and 197 $\rm arcmin^2$, respectively). A comparison of the maps is given in § 4.

4. SOURCE LIST

4.1. *Source Extraction*

Source extraction was performed on the PCA-cleaned, optimally filtered, coverage-normalized map consisting of all the raster scan observations co-added together. The algorithm was begun by doing a cut on the uniform coverage region, defined as the set of those pixels for which (1) the coverage is $\geq$70% of the maximum per pixel coverage and (2) the within-pixel rms is less than 2 σ from the mean within-pixel rms. The uniform coverage region is a contiguous region in the center of the map.

Next, an rms in sensitivity units (the flux density of each pixel times the square root of the integration time for that pixel in units of mJy $s^{1/2}$) was computed in the uniform coverage region. This rms is valid for the entire uniform coverage region since variations in coverage have been accounted for by the

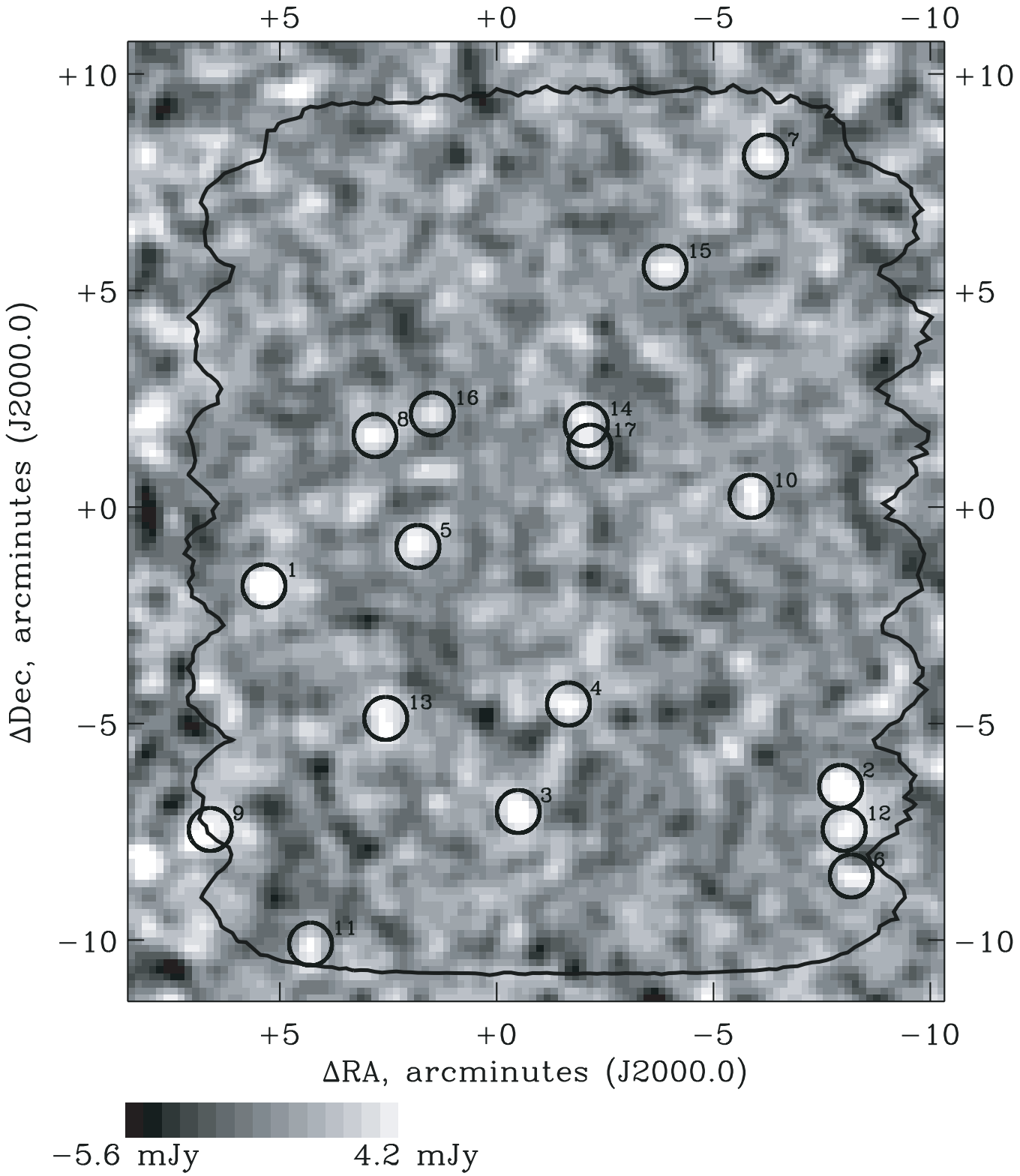

FIG. 5.—Bolocam map of the Lockman Hole East. The field is centered on R.A. = $10^{h}52^{m}08\overset{s}{.}82$, decl. = $+57^{\circ}21'33\overset{''}{.}80$ (J2000.0). The map pixels are $10'' \times 10''$, and the map rms is 1.4 mJy. The uniform, high-coverage region of the map is the inner 324 arcmin^2. This map has been cleaned and optimally filtered for point sources. The 17 Bolocam sources detected at >3 σ are indicated by thick circles. The bright spot at $+8'$, $-8'$ is not listed as a detection because it falls outside of the uniform coverage region (*black contour*).

$\sqrt{t_i}$ coverage normalization, where t_i is the total integration time for pixel i. All pixels with coverage-normalized flux densities exceeding 3 σ ("hot pixels") were flagged as potential sources. Then hot pixels were grouped into multipixel sources by making the maximal group of adjacent hot pixels, including those within $\sqrt{2}$ pixels (i.e., diagonally adjacent). The right ascension and declination of the source candidates were computed by centroiding two-dimensional Gaussians on the groups. Because convolution of the map with the Wiener filter properly weights the flux contribution from each pixel, the best estimate

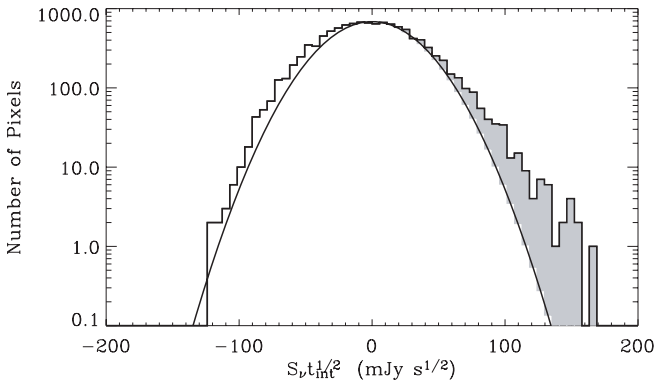

FIG. 6.—Histogram of the pixel sensitivities, defined as the pixel flux density, S_ν, times the integration time per pixel, $t_{int}^{1/2}$. The solid line is a Gaussian fit to the jackknifed histogram of Fig. 7. The shaded area indicates the emission due to galaxy candidates in excess of that expected from map noise. The negative side of the histogram is slightly broader than the fit to the jackknifed histogram owing to the presence of the galaxies (confusion noise) on both the positive and negative side. The small negative offset of the peak of the distribution is expected, as the mean of the entire map (and therefore the histogram) is constrained to have mean zero from both the high-pass filter in the Bolocam electronics and sky subtraction.

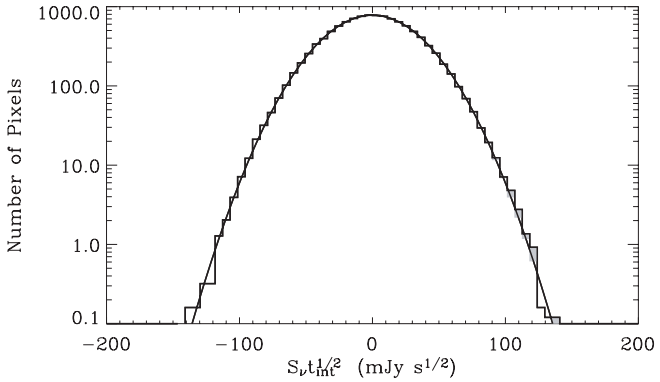

FIG. 7.—Jackknife histogram. In the jackknife test, 50% of the observations were randomly chosen and co-added together, while the remaining 50% of the observations were co-added into a second map. The two maps were then differenced. This was repeated 21 times with the observations randomly selected independently each time, and the histograms were averaged. The thick solid line corresponds to a Gaussian fit to the jackknifed histogram. The shaded region indicates the positive excess, which is insignificant.

of the source flux density in the optimally filtered map is given by the peak value in the group.

A histogram of the pixel values in the uniform coverage region is shown in Figure 6. The quantity that is plotted is the pixel sensitivity, with the scaling by $t_i^{1/2}$ accounting for the nonuniform coverage in the map. Note that the sensitivity histogram should not be interpreted as instrument sensitivity as the histogram uses an optimally filtered (smoothed) map but scales by sub–beam-sized integration times. The negative side of the histogram, plotted logarithmically, is extremely Gaussian. A Gaussian fit to the Bolocam noise-only (jackknife) distribution is overplotted by a solid line (see § 4.2), indicating a clear excess on the positive side with respect to the Gaussian. The galaxy candidates make up this excess. Since the pixels are $10'' \times 10''$ in size and the beam size is 0.30 arcmin^2, there are approximately 11 pixels per source candidate.

The source candidate list is presented in Table 2, where the flux densities are listed in order of decreasing brightness in the fifth column. Seventeen galaxy candidates were detected at $>3\ \sigma$ significance, with the brightest being 6.8 mJy. Seven of the candidates were detected at $>3.5\ \sigma$ significance. The flux densities of the source candidates were attenuated by the PCA cleaning; their corrected flux densities are listed (see § 3.2). The source candidate list is compared to the 850 μm SCUBA 8 mJy and 1.1 mm MAMBO surveys in § 4.3.

4.2. *Tests for Robustness of Galaxy Candidates*

Two tests were carried out to check the robustness of the galaxy candidates. The first test was a jackknife test in which 50% of the observations were randomly chosen and co-added together into a map and the remaining 50% of the observations were co-added into a second map. If the source candidates are real and coherent over multiple observations, then the positive-side excess of the histogram in Figure 6 should disappear when the two maps are differenced. Conversely, if the source candidates arise from spurious events in individual observations, such as cosmic-ray strikes, then the excess would not disappear when the two maps are differenced. This algorithm was repeated 21 times with the first 50% of the observations randomly selected independently each time, and the histograms were averaged. For such an algorithm, one expects the noise realizations to be approximately independent; the actual correlation was measured to be ~4%. The result is shown in Figure 7. A Gaussian distribution fits the jackknife histogram extremely well. The absence of a positive-side excess indicates that the source candidates in the Wiener-filtered map are common to all observations. The negative side of the real map histogram (cf. Fig. 6) is slightly broader because confusion noise from sources below our threshold is absent in the jackknife histogram. Similar histograms result from jackknife tests of scan direction (+R.A. vs. −R.A.), intranight variations (cuts on local sidereal time), and night-to-night variations, indicating that the galaxy candidates are not caused by systematic effects, such as scan-synchronous or elevation-dependent noise. This strong statistical test indicates that the Bolocam source candidates are real.

A second test was performed to verify that the source candidates arise from the co-addition of many observations rather than from spurious events. In this test, individual maps were made from each of the 259 observations. These maps were then co-added with fixed-amplitude offsets with random directions (phases). The expectation of this null test is that sources coherent over multiple observations are smeared out onto rings of a fixed radius, resulting in the disappearance of the positive-side excess. (The positive-side excess will be distributed over many pixels and therefore spread over many bins of the histogram.) Source candidates arising from isolated spurious events or characterized by length scales much larger than the Bolocam beam will merely be moved or negligibly broadened, leaving the histogram unchanged. Sixteen iterations were performed at each jitter amplitude ranging from $15''$ to $70''$ (Fig. 8). The rms of the jittered histograms in excess of the rms of the jackknife distribution of Figure 7 continues to decline out to a random jitter of $70''$. The excess does not go to zero at large amplitudes because the sources are spread out onto annuli with finite radii and will still be present at a low level. Since the area of the annulus increases as r, the excess should drop as r^{-1} (at large jitter amplitudes where the beams do not overlap), as indicated by Figure 8. This null test confirms that the excess variance (the positive-side excess in the histogram of Fig. 6 from source candidates) is contributed to by the ensemble of observations

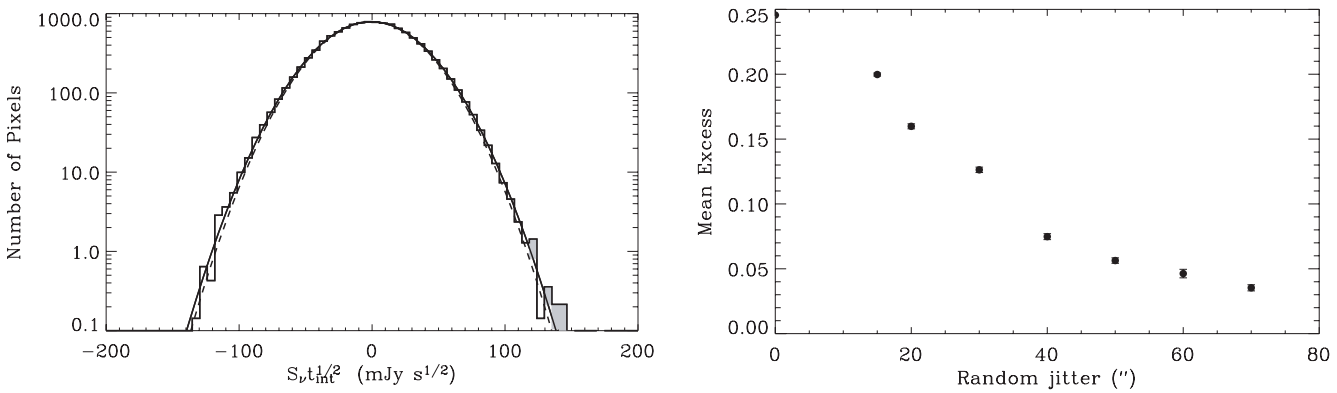

FIG. 8.—*Left*: Pointing-jittered histogram. In the pointing jitter test, individual maps were made from each observation, then co-added with 60″ amplitude offsets with random directions (phases). The solid line is a Gaussian fit to the negative side of the histogram and mirror imaged to the right side of the histogram, indicating that the galaxy candidates have disappeared. The dashed line corresponds to a Gaussian fit to the jackknifed histogram of Fig. 7. *Right*: Decreasing positive-side excess as a function of random jitter amplitude. In this case, the amplitude of the jitter was varied from 15″ to 70″. The excess is defined as the fractional increase in the rms of the jittered histogram compared to the rms of the jackknife distribution of Fig. 7. Sixteen iterations were performed at each jitter amplitude with the average plotted in the figure. The statistical uncertainty in each mean excess is smaller than the size of the plotted point.

and has a small characteristic length scale (corresponding to point sources).

4.3. *Comparison with Other Submillimeter and Millimeter-Wave Surveys*

The Bolocam galaxy survey provides a unique contribution to the current state of submillimeter galaxy surveys. The 850 μm JCMT SCUBA 8 mJy survey (Scott et al. 2002; hereafter SCUBA survey), with a 14″ beam, implemented a jiggle map strategy with a 30″ chop throw over 122 arcmin^2 to an rms of 2.5 mJy beam^{-1}. The 1.2 mm IRAM MAMBO survey (Greve et al. 2004; hereafter MAMBO survey), with a 10.″7 beam, scanned at 5″ s^{-1} with a chop throw of 36″–45″ and a chop frequency of 2 Hz over 197 arcmin^2 to an rms of 0.6–1.5 mJy beam^{-1}. Bolocam's 60″ s^{-1} raster scan strategy (without chopping) facilitated a large 324 arcmin^2 survey to a uniform rms of 1.4 mJy beam^{-1} (Wiener filtered for detection of point sources). Using a model SED based on nearby, dusty, star-forming galaxies (see § 6.3) gives relative flux densities of 1 : 2.0 : 0.8 and relative rms of 1 : 0.9 : 0.6–1.4 for the Bolocam, SCUBA, and MAMBO surveys, respectively, for a galaxy redshift of $z = 2.4$ (with the range given for MAMBO due to nonuniform noise).

Figure 9 provides a cumulative overview of recent far-infrared, submillimeter, and radio observations of the Lockman Hole. The circles of Bolocam, SCUBA, and MAMBO observations correspond to 2 σ confidence regions of position, including both beam sizes and stated pointing errors. The 6 cm VLA radio sources of Ciliegi et al. (2003) and unpublished 21 cm VLA sources of M. Yun (2004, private communication), with average noise levels of 11 and 10–15 μJy beam^{-1}, respectively, are identified. The M. Yun (2004, private communication) radio field covers the entire Bolocam good coverage region, while the center of Ciliegi et al. (2003) observations is offset to the northwest, with an overlap of approximately 130 arcmin^2. Also shown are the 20 published radio sources from deep 21 cm VLA observations (average noise level of 4.8 μJy beam^{-1}) from Ivison et al. (2002) that are coincident with SCUBA sources, as well as an additional 21 cm VLA source discovered by Egami et al. (2004) from the reexamination of the Ivison et al. (2002) map. Infrared detections from a recent wide-field 95 μm ISOPHOT survey (Rodighiero & Franceschini 2004) and recent *Spitzer* detections of SCUBA sources (Egami et al. 2004) are also identified. Five SCUBA sources from the Scott et al. (2002) catalog (LE850.9, 10, 11, 15, 20) were retracted by Ivison et al. (2002) on the basis of large $\sigma_{850\ \mu m}$ values (and lack of radio identifications) and are depicted by crosses through them.

Examination of Figure 9 shows discrepancies in detections between the surveys. Table 3 summarizes the coincident detections between Bolocam 1.1 mm, SCUBA 850 μm, MAMBO 1.2 mm, and VLA radio observations. Each row in the table corresponds to the fractional number of counterparts detected by each survey. The five SCUBA sources retracted by Ivison et al. (2002) are not included in this comparison. The coverage of each survey was taken into account, with only the overlapping uniform coverage regions considered. The surveys have a wide range of agreement, ranging from 23% (7 of 31 SCUBA sources detected by Bolocam) to 75% (6 of 8 Bolocam sources detected by SCUBA). Six of the 17 Bolocam detections are galaxies previously detected by the SCUBA 8 mJy survey. Of the remaining 11 Bolocam sources, 9 of them lie outside the SCUBA 8 mJy survey region. Similarly, 7 of the 11 Bolocam sources present within the MAMBO good coverage region were detected with MAMBO at 1.2 mm. Two of the 4 Bolocam source candidates not detected by MAMBO have expected 1.2 mm flux densities (from the model SED of § 6.3) below the MAMBO detection threshold for $z = 2.4$. The large fraction of Bolocam sources detected by SCUBA and MAMBO suggests that these submillimeter galaxy candidates are real. The impact of the converse of this statement is less clear: The majority of SCUBA and MAMBO sources were not detected by Bolocam, although 17 out of 24 nondetected SCUBA sources and 7 out of 15 nondetected MAMBO sources have expected 1.1 mm flux densities (from the aforementioned model SED) below the Bolocam detection threshold, nor is there a strong correlation between SCUBA and MAMBO sources. Some of these sources may not be real or may not be modeled well by the assumed SED. Furthermore, the majority (65%) of Bolocam source candidates have at least one radio coincidence (Ivison et al. 2002; Ciliegi et al. 2003; M. Yun 2004, private communication), although a 34% accidental detection rate is expected. (This accidental detection rate is the Poisson likelihood that one or more of these known radio sources, randomly distributed, fall within the 2 σ confidence region of the Bolocam beam.) To help verify the 9.″1 pointing rms of § 3.3, the rms positional error of the Bolocam

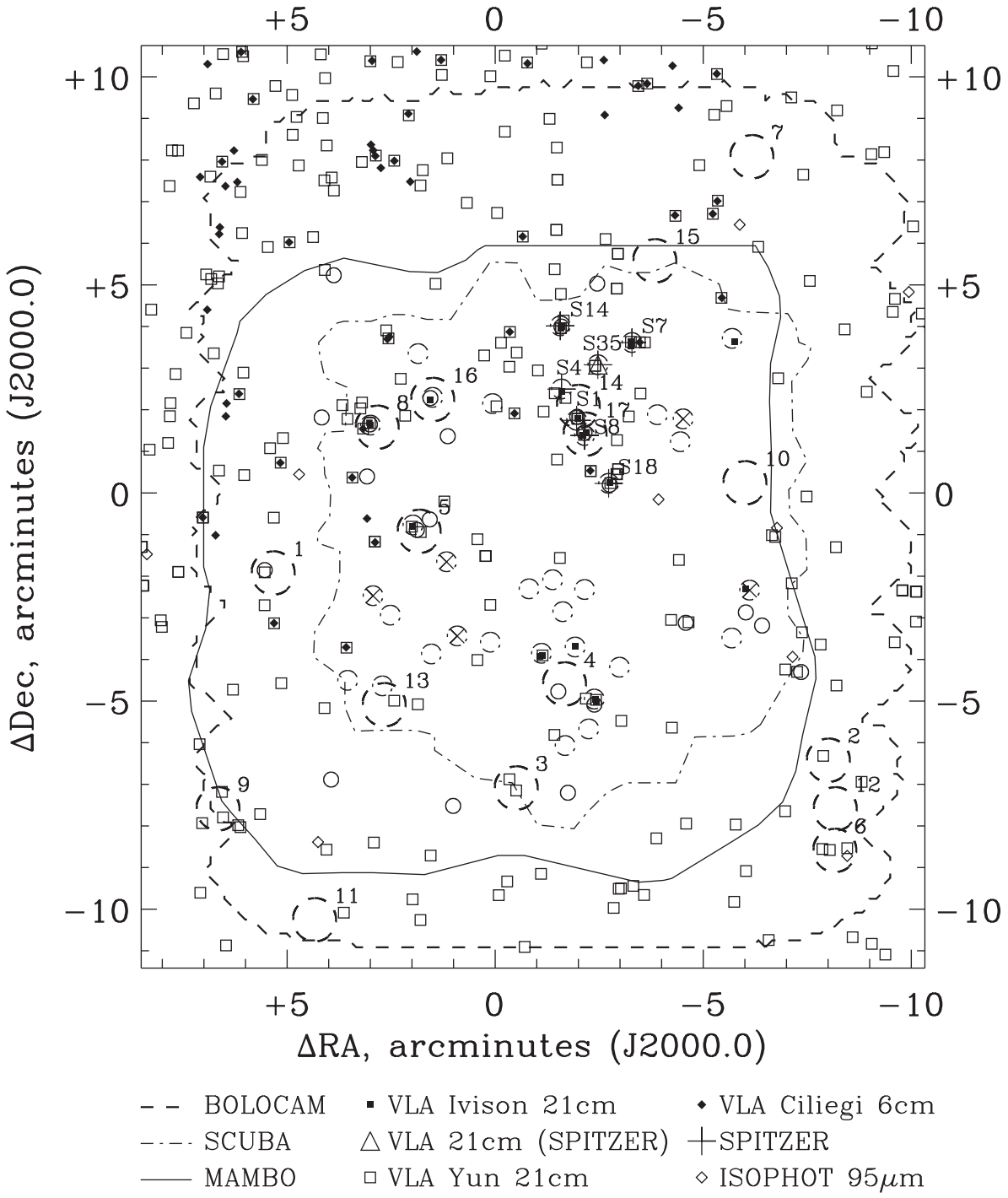

FIG. 9.—Galaxy surveys in the Lockman Hole East region. The 17 Bolocam submillimeter galaxy candidates have been labeled in order of brightness. The circle radii of Bolocam, SCUBA (Scott et al. 2002), and MAMBO (Greve et al. 2004) detections correspond to twice the beam sizes and stated pointing errors added in quadrature to indicate an approximate region of astrometric uncertainty and source confusion. The good coverage regions of Bolocam, SCUBA, and MAMBO are shown. VLA radio sources of Ciliegi et al. (2003), M. Yun (2004, private communication), and Ivison et al. (2002) are identified by filled diamonds, open squares, and filled squares, respectively. The five crossed-out SCUBA sources are those retracted by Ivison et al. (2002). Open diamonds correspond to 95 μm ISOPHOT detections of Rodighiero & Franceschini (2004). Plus signs correspond to SCUBA sources detected by *Spitzer* IRAC and/or MIPS observations (Egami et al. 2004). Reexamination of the 20 cm Ivison et al. (2002) VLA radio map by the *Spitzer* group (Egami et al. 2004) reveals a source (*triangle*) coincident with SCUBA source LE850.35.

galaxy candidates compared to the VLA radio positions was calculated for both all Bolocam sources with radio counterparts and the subset of sources (1, 5, 8, 16, and 17) with additional SCUBA and/or MAMBO detections. (Bolocam galaxy candidate 14 was excluded owing to source confusion.)

Five of the Bolocam source candidates show no counterparts in the other surveys. These may be false detections, although four of these candidates are near the edge or outside of the SCUBA and MAMBO good coverage regions, which may explain the lack of additional submillimeter detections. It is possible that one or more of these four Bolocam source candidates without radio counterparts may instead be sources at high redshift ($z > 3$), where the positive K-correction (sharp drop in flux density with increasing redshift) causes dim radio counterparts. Four SCUBA

TABLE 3
Summary of Coincident Detections

Survey	Fraction of Galaxy Candidates Detected				Accidental Radio
	Bolocam	SCUBA	MAMBO	Radio	
Bolocam/CSO	...	6/8	7/11	12/17	6
JCMT SCUBA	7/31	...	8/31	15/31	3
IRAM MAMBO	8/23	8/17	...	11/23	1

Notes.—Each row corresponds to the fraction of sources detected *by* each survey (i.e., 6 of 8 Bolocam galaxy candidates in the overlap region were detected by SCUBA, whereas Bolocam detected 7 of 31 SCUBA sources). Column of radio detections includes detections by Ivison et al. (2002), Ciliegi et al. (2003), and/or M. Yun (2004, private communication). The accidental detection rate is that expected from a random distribution of these known radio sources within the 2 σ confidence regions of Fig. 9.

detections that have at least two detections from MAMBO, *Spitzer*, and VLA were not detected by Bolocam, although the corresponding pixels in the Bolocam map have flux values just below the 4.2 mJy detection threshold for two of these nondetections. A description of each Bolocam detection (as well as nondetections) follows in the next section. A follow-up paper is in preparation that will include a more detailed discussion on individual sources, including redshift/temperature constraints.

The Bolocam 1.1 mm beam solid angle is 0.30 arcmin^2, and the uniform coverage region of the map is 324 arcmin^2. There are thus approximately 1000 beams in the map. With 17 source candidates, or $\sim$50 beams per source, source confusion is not a serious issue. We define ''source confusion'' here as a high spatial density of detected sources that makes it difficult to distinguish individual sources. This should not be confused with ''confusion noise'' from sources below the detection threshold (discussed in detail in § 5.4). Nevertheless, source confusion exists at some level because several Bolocam sources are either closely spaced or near multiple SCUBA detections. While the clustering properties of submillimeter galaxies remain uncertain, there exists tentative evidence from both two-dimensional angular correlation functions (Greve et al. 2004; Scott et al. 2002; Borys et al. 2003) and clustering analyzed with spectroscopic redshift distributions (Blain et al. 2004) that suggests strong clustering with large correlation lengths (as well as correlation to other classes of high-redshift galaxies, including Lyman break galaxies and X-ray loud AGNs; Almaini et al. 2003). We do not attempt to quantify source confusion here but address it in a paper in preparation.

There are 24 8 mJy SCUBA 850 μm and 15 MAMBO 1.2 mm sources within our survey region that we did not detect. Statistically, however, we detect the aggregate average of these at significances of 3.3 and 4.0 σ, respectively, at $\lambda = 1.1$ mm. This was done by measuring the distribution of ''sensitivity'' values (scaled by $t_i^{1/2}$) for the Wiener-filtered map pixels that coincide with SCUBA or MAMBO sources for which we found no excursion above our detection threshold. If no subthreshold ''counterparts'' are present in these pixels, the sensitivity values should follow the noise distribution of the map (albeit truncated at 3 σ). Such a distribution has a mean value of -0.004 σ. In the data, we find that the sensitivity values for these map pixels have mean values of 1.0 ± 0.3 and 0.8 ± 0.2 σ for the SCUBA and MAMBO nondetections, respectively. Assuming that uncertainties are Gaussian distributed, the probabilities of such large nonzero means to have arisen from pure noise are very low, 1.7×10^{-4} and 2.5×10^{-4}, respectively. Thus, we have statistically detected the ensemble of SCUBA and MAMBO sources below our threshold at the 3.3 and 4.0 σ confidence levels, respectively.

4.4. *Bolocam Detections*

The Bolocam detections are as follows:

Bolocam.LE1100.1.—This 6.8 mJy galaxy candidate has Bolocam and MAMBO detections but falls outside of the region covered by SCUBA observations. A strong 20 cm VLA radio observation (M. Yun 2004, private communication) exists within both the Bolocam and MAMBO confidence regions.

Bolocam.LE1100.2.—This 6.5 mJy Bolocam detection has a coincident 20 cm radio (M. Yun 2004, private communication) detection. The source lies outside good coverage regions of the SCUBA, MAMBO, and Ciliegi et al. (2003) VLA observations.

Bolocam.LE1100.3.—This source has a 6.0 mJy Bolocam detection with two 20 cm radio (M. Yun 2004, private communication) plausible counterparts but lacks a MAMBO detection. The source lies outside the good coverage regions of the SCUBA and Ciliegi et al. (2003) VLA observations.

Bolocam.LE1100.4.—This 5.2 mJy galaxy candidate has Bolocam and MAMBO detections with no SCUBA or radio detections. Several SCUBA sources (with radio counterparts) are in close proximity to this source; however, the coincident MAMBO source (with a comparatively small 10$''$.7 beam FWHM) confirms the Bolocam detection at this location.

Bolocam.LE1100.5.—This 5.1 mJy galaxy candidate has Bolocam, SCUBA, and VLA (Ivison et al. 2002) detections with two coincident MAMBO and M. Yun (2004, private communication) detections.

Bolocam.LE1100.6.—Bolocam detection 6 (5.0 mJy) has three potential 20 cm VLA radio counterparts (M. Yun 2004, private communication) and a 95 μm ISOPHOT (Rodighiero & Franceschini 2004) detection within the Bolocam confidence region. No SCUBA or MAMBO coverage (or Ciliegi et al. [2003] VLA coverage) exists for this detection.

Bolocam.LE1100.7, 10, 11, 12, 15.—These five sources (4.9, 4.7, 4.6, 4.6, and 4.4 mJy, respectively) are Bolocam galaxy candidates with no other coincident detections (including radio counterparts), although sources 7, 11, 12, and 15 fall near the edge or outside of the SCUBA, MAMBO, and VLA (Ciliegi et al. 2003) good coverage regions. These sources may be false detections, since six are statistically expected from simulations (see § 5), or possibly galaxies at high redshift ($z > 3$). The likelihood of sources 10, 11, 12, and 15 being false detections is enhanced by the fact that their flux densities are near the 4.2 mJy threshold.

Bolocam.LE1100.8, 16.—These submillimeter galaxies have Bolocam (4.8 and 4.1 mJy, respectively), SCUBA, MAMBO, and VLA (8, 16, Ivison et al. 2002; 8, Ciliegi et al. 2003; 8, M. Yun 2004, private communication) detections.

Bolocam.LE1100.9.—This galaxy candidate has a 4.8 mJy Bolocam detection with three 20 cm radio detections (M. Yun 2004, private communication) within the Bolocam confidence region. There is no SCUBA, MAMBO, or Ciliegi et al. (2003) VLA coverage in this region.

Bolocam.LE1100.13.—This 4.5 mJy Bolocam detection has SCUBA and VLA radio (M. Yun 2004, private communication) counterparts but no Ivison et al. (2002) or Ciliegi et al. (2003) VLA detections.

Bolocam.LE1100.14, 17.—These two closely spaced Bolocam detections (4.4 and 4.0 mJy, respectively) have numerous other detections, including three SCUBA sources, two MAMBO sources, and multiple VLA radio sources (S1, S4, S8, Ivison et al. 2002; S1, S4, S8, M. Yun 2004, private communication). *Spitzer* detections with IRAC at 3.6, 4.5, 5.8, and 8.0 μm exist for all three SCUBA sources, as well as 24 μm detections with MIPS for SCUBA sources 1 and 8. (Three IRAC and MIPS sources are seen within a radius of 8″ of SCUBA source 8.) Because of the 31″ size of the Bolocam beam, we are likely influenced by source confusion.

4.5. *Bolocam Nondetections*

The Bolocam nondetections are as follows:

SCUBA.LE850.14, 18.—These galaxy candidates have SCUBA and MAMBO detections, with *Spitzer* IRAC and MIPS and VLA (Ivison et al. 2002, M. Yun 2004, private communication) counterparts. SCUBA source 14 is discernible in the Bolocam observations at 3.9 mJy, just below the 4.2 mJy, 3 σ detection threshold. The Bolocam pixel coincident with SCUBA source 18 has a flux density of 1.6 mJy, well below the detection threshold.

SCUBA.LE850.7, 35.—These sources are detected by SCUBA, *Spitzer* IRAC and MIPS, and VLA (7, Ivison et al. 2002; 7, 35, M. Yun 2004, private communication; 7, Ciliegi et al. 2003; 35, Egami et al. 2004). The flux density in the Bolocam map coinciding with SCUBA source 7 is 3.4 mJy, below the 3 σ detection threshold. At a Bolocam flux density of 0.9 mJy, SCUBA source 35 is well into the Bolocam noise.

5. NUMBER COUNTS

In this section we discuss the extraction of the number (per unit flux density per unit solid angle) versus flux density relation ("number counts") from the observed sources. Because of the presence of noise (due to the instrument, the atmosphere, and confused background sources), there is a bias in both the observed flux densities and the observed histogram of number of sources versus flux density. This bias, first noted by Eddington (1913, 1940), is quite generic when attempting to measure a statistical distribution in the presence of noise. Further, because our S/N with respect to these noise sources is not large, this bias is an effect comparable in size to the statistical Poisson errors in determining the number counts.

There are two broad approaches to extracting the number counts in the regime where bias is significant. The first is to directly correct the observed number versus flux histogram using some knowledge of the statistics of the survey. The other approach is to assume a model and attempt to match its parameters to the data using a fit, aided by simulation. The direct correction approach does not appear promising for this survey. Eddington (1940) showed that, in the presence of Gaussian measurement noise, one could apply an asymptotic series correction to the observed distribution to obtain a better estimate of the underlying distribution. This correction involves even-numbered derivatives of the observed distribution, and so, with our observed distribution containing only 17 sources, this method is impractical. Another approach might be to individually correct each source by its expected bias, but Eddington (1940) also showed that using the distribution of corrected fluxes as a measure of the underlying distribution is fundamentally incorrect. Thus, we have elected to fit a model to the data.

The formalism for relating a given underlying number count distribution to the observed number counts is given in § 5.1. This provides the definition of the survey bias, completeness, and false detection rate. The simulations used to determine these quantities are described in § 5.2, and their actual calculation is given in § 5.3. The effect of confusion noise on the survey is discussed in § 5.4. The method of extracting the underlying counts is given in § 5.5. Caveats and difficulties in extracting the underlying number counts, as well as suggestions for improvements in a future analysis, are discussed in § 5.6.

5.1. *Formalism*

For a given observing frequency band, we denote the differential number count (DNC) distribution of galaxies per unit flux density interval per solid angle as $N'(S)$. The cumulative number count (CNC) distribution will be denoted $N(S)$, with units of number per solid angle. The relation between the true N' and the observed distribution n' must account for the effects of random noise, the presence of a detection threshold, and confusion noise (i.e., a contribution to the variance of the map due to sources below the detection threshold). As a result of all forms of noise, a source having flux density S is in general observed with a different flux density s. Let $B(s, S; N')$ be the probability density that a source with true flux density S is observed at a flux density s; the implicit dependence on the confusion noise is included by the parametric dependence on N'. $B(s, S; N')$ is normalized such that

$$\int_{-\infty}^{\infty} B(s,\ S;\ N')\, ds = 1 \tag{2}$$

for all values of S. The quantity $B(s, S; N')$ will be referred to as the "survey bias." By normalizing according to equation (2), one assumes that a source of true flux S will be found at some flux s with probability unity. In the presence of a detection threshold, however, sources whose observed flux fluctuates below the threshold will not be included in n'. In this case, the integral in equation (2) is not 1, but $C(S; N')$, the "survey completeness," namely, the probability that the source is found at all. Note that this also depends on the confusion noise through N'. In addition, there may be *false detections* of noise fluctuations, $F(s)$, which contribute to the observed number counts. Thus, the expression for the observed DNC distribution is

$$n'(s) = F(s) + \int_0^{\infty} B(s,\ S;\ N')C(S;\ N')N'\, dS. \tag{3}$$

In the following, the dependence of B and C on N' will not be written explicitly.

Under the assumptions of uniform Gaussian noise with rms σ, negligible contribution from confusion noise, and a fixed

detection threshold $n\sigma$, analytical expressions for $C(S)$, $B(s, S)$, and $F(s)$ can be derived. For future reference, these are

$$C(S) = \frac{1}{\sqrt{2\pi}\sigma} \int_{m\sigma}^{\infty} \exp\left[\frac{-(s-S)^2}{2\sigma^2}\right] ds, \quad (4)$$

$$B(s,\ S) = \frac{1}{C(S)} \frac{1}{\sqrt{2\pi}\sigma} \exp\left[\frac{-(s-S)^2}{2\sigma^2}\right] \Theta(s - m\sigma), \quad (5)$$

$$F(s) = \frac{\mathcal{N}}{\sqrt{2\pi}\sigma} \exp\left(\frac{-s^2}{2\sigma^2}\right) \Theta(s - m\sigma), \quad (6)$$

where $\Theta(x)$ is the unit step function ($\Theta = 1$ for $x > 0$, $\Theta = 0$ for $x < 0$) and $\mathcal{N}$ is a normalization factor for $\mathcal{N}$ independent noise elements.

5.2. *Simulation of Noise Maps*

Two types of simulations were done to determine the survey bias, completeness, and false detection rate. Both methods simulate only the instrument and atmospheric noise (the "random noise") and do not include the effect of confusion noise. This is appropriate for the case in which the random noise dominates. The validity of this assumption is discussed in § 5.4.

In the first suite of simulations, the observational data were used to generate 100 fake maps (noise realizations) by jittering the individual time streams 60″ in right ascension/declination coordinates with a random phase before they were co-added to make maps. This had the effect of washing out the point sources as discussed in § 4.2. Note that realizations of these jittered maps are not fully independent because the noise is somewhat correlated between realizations; the average correlation coefficient between maps is 4%. Statistical error bars on the completeness and bias determined from this simulation method include the contribution from the correlation. The pointing jitter dilutes the variance of sources present in the jittered map to 20% or less of its value in the unjittered map (see Fig. 8), effectively removing confusion noise.

Because of the large amount of time required to generate many realizations of maps from real time stream data (as in the case of the jittered maps) and the difficulties of fully simulating time stream realizations of instrument and atmospheric noise, a second simulation method was developed. In this method, the noise properties are derived from the jackknife maps, which represent realizations of signal-free instrument noise. The noise model for the map (before optimal filtering) assumes that the noise map, $n(\boldsymbol{x})$, can be described as an independent noise per pixel that scales as $1/\sqrt{t_i}$, where t_i is the integration time in pixel i, combined with a mild pixel-to-pixel correlation. This correlation is assumed to be stationary over the map and can thus be described by the two-dimensional PSD of the noise map $\xi^2(\boldsymbol{k})$, normalized so that its integral has unit variance. These assumptions are justified because, as shown in § 4, the coverage variation accounts for most of the point-to-point variation in the noise, and examination of the jackknife map PSD shows that the $1/k$ contribution to the PSD is small compared to the white term, leading to largely uncorrelated pixels. The noise model for the map after Wiener filtering is straightforwardly obtained by convolving the noise map with the Wiener filter.

The assumptions above are equivalent to writing the covariance matrix $\boldsymbol{C}$ for the unfiltered map as

$$\boldsymbol{C} = \boldsymbol{D}^{1/2} \mathcal{F}^{-1} \xi^2 \mathcal{F} \boldsymbol{D}^{1/2},$$

where $\boldsymbol{D}$ is diagonal in pixel space and describes the coverage variations, ξ is diagonal in $\boldsymbol{k}$-space and describes the pixel noise correlations, and $\mathcal{F}$ is the discrete Fourier transform. The elements of $\boldsymbol{D}$ can be written as

$$D_{ij}^{1/2} = \sqrt{\frac{A}{t_i}} \sigma \delta_{ij},$$

where σ^2 is the sample variance of the noise and A is a normalization that ensures that the sum of the pixel variances $\sum_i A\sigma^2/t_i$ is equal to $(N-1)\sigma^2$, the total noise variance in the map. The noise map should satisfy $\langle nn^T \rangle = \boldsymbol{C}$; a given realization is

$$n = \boldsymbol{D}^{1/2} \mathcal{F}^{-1} \xi \mathcal{F} w,$$

where w is a realization of uncorrelated, Gaussian, mean zero, unit variance noise. Determining the noise model then reduces to determining the form of $\xi(\boldsymbol{k})$ and the value of σ. The PSD ξ^2 is computed directly from the uniform coverage region of the unfiltered jackknife maps using the discrete Fourier transform; multiple jackknife realizations (which are nearly independent) and adjacent $\boldsymbol{k}$-space bins are averaged to reduce the noise on the measurement of the PSD. The overall noise normalization σ is determined by requiring that the variance of $n(\boldsymbol{x})$, when considered in the good coverage region, Wiener filtered, and multiplied by $\sqrt{t_i}$, is equal to the variance similarly determined from the jackknife maps (§ 4.2 and Fig. 7). One thousand noise realizations were generated in this way.

5.3. *Calculations of False Detection Rate, Bias, and Completeness*

The false detections were determined by simply running the source detection algorithm on each of the simulated maps for both types of simulations and recording the number and recovered flux density of the detections. Figure 10 shows the results for both methods. Also plotted is the theoretical prediction, assuming that the normalization $\mathcal{N}$ is either $N_{\rm beams}$ or $N_{\rm pixels}$, which should bracket the possibilities. It is seen that neither Gaussian model describes the simulated false detection rate well, although both methods of simulation agree well with each other. The Gaussian model does not describe the simulation data well in either amplitude or shape. The amplitude discrepancy occurs because $\mathcal{N}$ is the number of effective independent noise elements, which depends on both the correlations in the noise and the detection algorithm, which does not count all pixels above threshold as source candidates but considers all pixels within a merged group to be a single source. The shape of the Gaussian model fits poorly owing to three effects: First, because of the coverage variation, the threshold is not sharply defined in flux density units, causing some false detections *below* the threshold. Second, the grouping algorithm merges closely spaced false detections in the Wiener-filtered map and assigns a single flux density to the brightest pixel, a conditional probability that is flux dependent. Finally, the pixels are not independent, since both $1/f$ noise and the Wiener filter correlate them. Because of the difficulty in deriving an analytic expression for all these effects, the false detection rate as determined by simulation is used in further analysis (see § 5.5) instead of the Gaussian prediction. The mean number of false detections in the Lockman Hole map as determined from simulation is 6 (Poisson distributed).

To find the completeness and bias, sources of known flux density were injected into the noise maps. First, a source-only

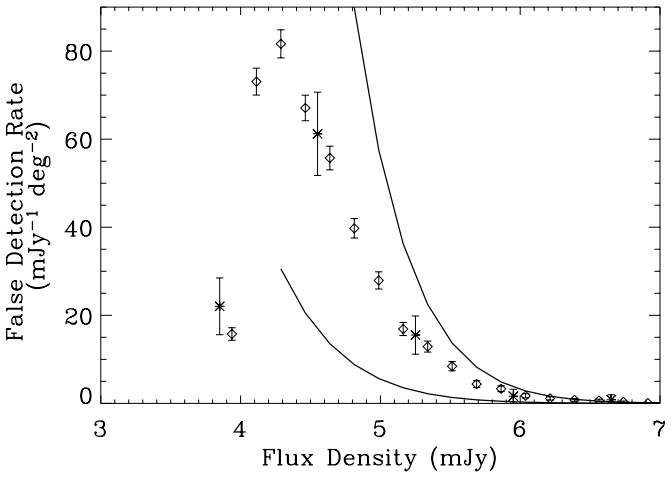

FIG. 10.—False detection rate plotted vs. flux density. Diamonds are simulations from the map statistics, and asterisks are simulations from the data, shown with error bars for the finite number of simulation realizations. The two solid curves show the theoretical bounds on this quantity, the lower curve assuming that the number of independent statistical elements is the number of beams in the map, and the upper assuming that it is the number of pixels in the map.

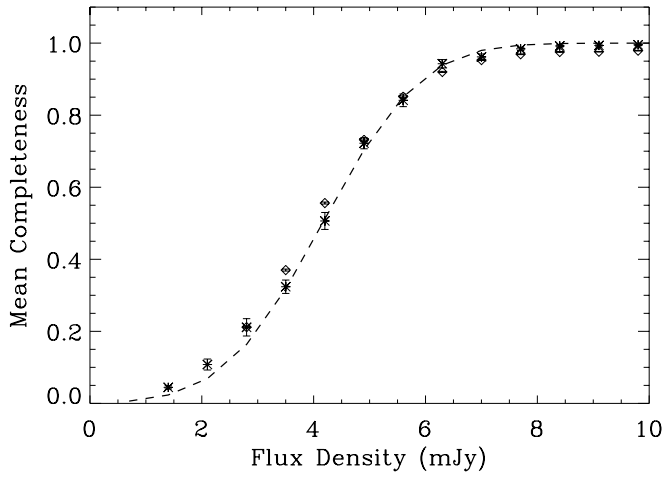

FIG. 11.—Survey completeness as a function of flux density. Diamonds are simulations from the map statistics, and asterisks are simulations from the jittered data, shown with error bars for the finite number of simulation realizations. The dashed curve shows the theoretical prediction for the Gaussian case with $\sigma = 1.4$ mJy (the mean noise level of the cleaned Lockman Hole map). The error bars are statistical only and do not reflect systematic differences in the two simulation methods.

map was created by adding 30 31″ FWHM two-dimensional Gaussians at a specified flux density level to a blank map. The sources were injected at random into the uniform coverage region but were spaced far enough apart that the source detection algorithm could distinguish each of them; this circumvented potential complications involving source confusion. Then, the source-only map was added to a noise map to simulate a sky map post cleaning and mapping. Next, this map was Wiener filtered and run through the source extraction algorithm, which enabled us to determine which sources were detected and their resulting flux densities. Each extracted detection was centroided to determine its position, and then its position was compared with the position of the nearest injected source. If the positions were within 15″ (roughly the distance between two adjacent, diagonal pixels), the extracted detection was considered real. The flux density was determined by the maximum value of detected pixels, as is appropriate for the Wiener-filtering algorithm.

With these mechanics in place, the completeness was calculated by computing the ratio of the number of detections at a given flux to the number of injected sources. This was repeated for source flux densities ranging from 2.8 to 9.8 mJy for simulations from map statistics and from 1.4 to 9.8 mJy for jittered data simulations in 0.7 mJy intervals, with the results plotted in Figure 11. The two types of simulations agree well. The survey completeness is 50% at the 3 σ detection threshold, as expected, because half of the sources at the threshold will be bumped upward by noise and half will be bumped downward. The simulations also agree with the theoretical prediction for Gaussian noise.

The bias was computed by determining the distribution of measured flux densities as a function of injected flux densities. At relatively large flux densities, the bias distribution should approach a Gaussian distribution centered at the injected flux density, with σ equal to the map rms. This is seen to be the case in Figure 12 for injected flux densities $\geq$7 mJy. The figure gives the distribution of the expected observed flux densities (probability density per flux bin, normalized to an integral of unity) for a range of injected flux densities. For low injected flux densities approaching the detection threshold, the distributions become increasingly asymmetric owing to the presence of the threshold. The distributions do not drop abruptly to zero below the threshold because there are variations in the map coverage. Note that sources with true flux below the detection threshold may be detected. The average bias for a source is shown in Figure 12; this rises steeply for sources with fluxes near or below the detection threshold.

The preceding discussion (in particular the agreement of the simulated bias and completeness with the Gaussian theoretical prediction) indicates that, in spite of coverage variations and correlated noise, the noise in this survey behaves substantially like uniform Gaussian noise. Comparison of the results of the map simulation method with the jitter technique also shows good agreement, indicating that the assumptions that went into the map simulation method are justified and that we have a reasonable model for the survey noise. This gives added confidence to the determination of the false detection rate, which depends only on the noise properties.

5.4. *Effects of Confusion Noise on the Bias and Completeness Functions*

The completeness and bias function estimates as determined in §§ 5.2 and 5.3 do not include the effects of confusion noise. The effect of confusion noise is illustrated by considering two extremes: instrument noise dominant over confusion noise and vice versa. When instrument noise is dominant, the bias function for this survey is correctly described by equation (5). In the confusion-dominated limit, the bias function takes on the shape of the source count distribution, reflecting the fact that it is the underlying distribution of sources that may bias the flux of a given source. In between these two extremes, the Gaussian bias function acquires additional width and a long positive tail from the source counts distribution. This tail increases the probability that a low flux source will fluctuate above the detection threshold. Consequently, the completeness at low flux densities is increased over the case of Gaussian noise. Note that small changes in the bias tail can cause large changes in the subthreshold completeness. The case at hand falls in this in-between regime. Understanding the modification to the bias function by confusion noise is necessary for accurately estimating how confusion transforms a model source count distribution to an

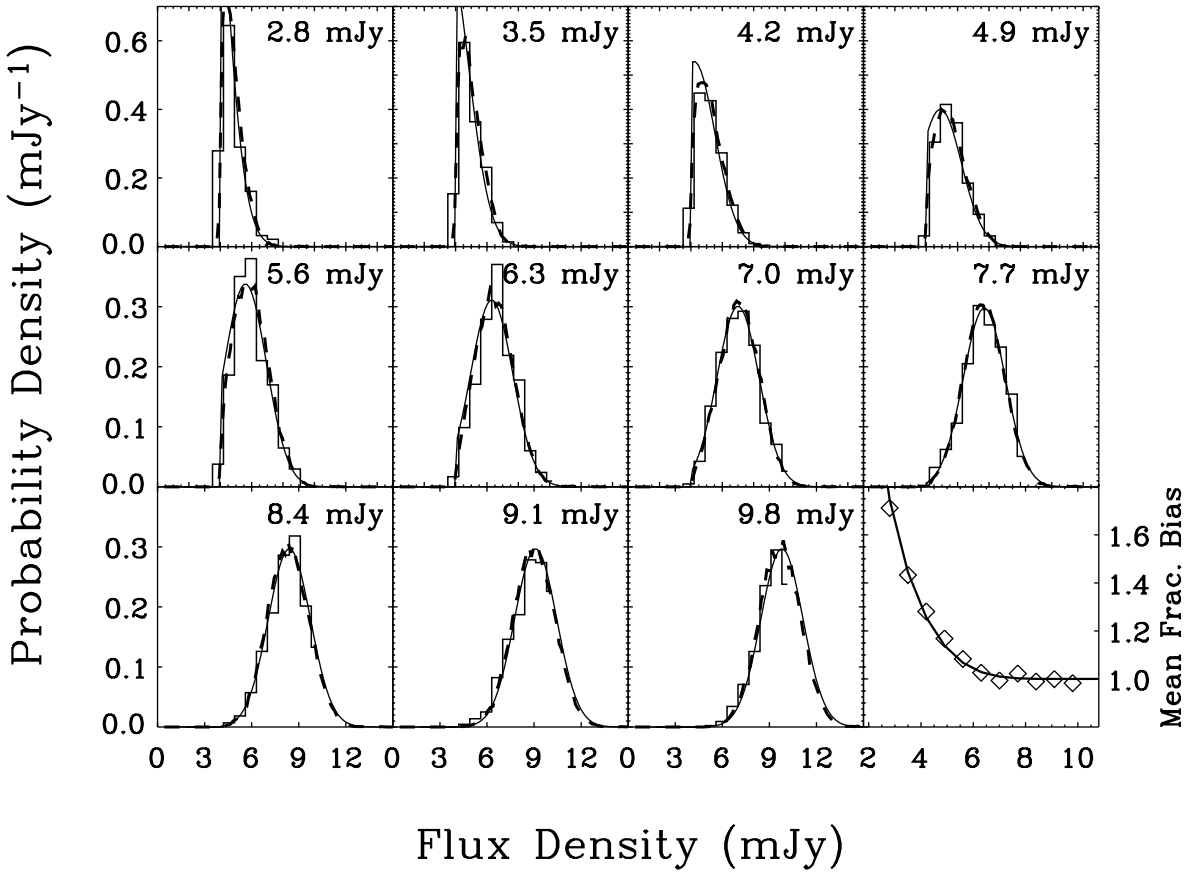

FIG. 12.—Survey bias as a function of observed flux density for a variety of input flux densities. The bias is normalized as a probability density as a function of observed flux density. The flux densities of the sources injected in the simulation are shown in the top right of each panel. The solid histograms are simulations from the jittered data, the dashed curves are simulations from the map statistics, and the solid curves (which lie nearly on top of the map statistics simulation) are the Gaussian predictions for $\sigma = 1.4$ mJy (the mean noise level of the cleaned Lockman Hole map). The bottom right panel shows the mean fractional bias as a function of input flux density for the simulations from the map statistics. The solid curve is the Gaussian prediction for $\sigma = 1.4$ mJy.

observed one, as in equation (3). It is difficult to precisely model the effects of confusion on bias and completeness because they depend on the source count distribution that one is trying to measure.

We can estimate the size of the confusion noise present in our maps by finding the relative contributions of the noise and signal variances. The sample (per pixel) variance of the optimally filtered Lockman map in the good coverage region is found to be 2.37 mJy^2. The variance of the optimally filtered jackknife maps in the same region is 1.81 mJy^2, leaving 0.56 mJy^2 due to sources. The variance contributed by all the sources in Table 2 is approximately 0.33 mJy^2, of which 0.10 mJy^2 is expected to be due to false detections of random noise peaks. This leaves 0.33 mJy^2 due to undetected sources. This represents an S/N per pixel of 0.37 in rms units; considered in quadrature with the 1.81 mJy^2 of the noise, it increases the noise estimates and the rms of the bias function by about 9%.

To estimate the effect of confusion noise on the survey completeness and bias, particularly in the tail, sources were injected one at a time into the real map and extracted using the source extraction algorithm, with the completeness and bias calculated as in the noise-only case. This has the effect of making only a small change in the observed distribution of pixel values, effectively preserving that distribution. No effort was taken to avoid the positions of source candidates, as this would bias the procedure by failing to take into account the tail of the distribution. This test showed that the bias acquired a high flux density tail, as expected, and the completeness was increased above its Gaussian noise value. It should be emphasized, however, that this method provides an upper limit because it effectively "double-counts" confusion: the map into which the sources are injected is already confused. Positions of high flux in the true map may already consist of two coincident lower flux sources, and so the probability of a third source lying on top of them is not truly as high as the probability we would calculate by this procedure. The determination of the completeness and bias in this way is also limited by the statistics of only having one realization of the confusion noise. Applying these new bias and completeness functions, as well as the Gaussian noise–only bias and completeness (eqs. [4] and [5]), to a power-law model of the number counts (the best-fit model of § 5.5), the change in the observed counts is of order the size of the 68% confidence interval for Poisson errors in the observed counts. Thus, confusion noise is not wholly negligible nor does it dominate. In extracting the number counts, we ignore the confusion noise but discuss how to treat it correctly in § 5.6.

5.5. *Fitting a Model to the Differential Number Counts*

To extract number counts from this data set, we use equation (3) with the simulation-derived false detections and the completeness and bias of equations (4) and (5). A model for N' is also required. Because of the small number of detections, the model must have as few free parameters as possible so that the data will be able to constrain the model parameters. This pushes us away from detailed, physically motivated models and toward a simple model in combination with several, somewhat

arbitrary, constraints. We use a two-parameter power-law model for N' given by

$$N'(S;\ \boldsymbol{p}) = A\left(\frac{S_0}{S}\right)^{\delta}, \tag{7}$$

where $\boldsymbol{p} = [A,\ \delta]$ and S_0 is a fixed constant (not a parameter of the model). The choice of this form for $S_0 \neq 1$ reduces the degeneracy between A and δ that prevails over narrow ranges of S, such as in this survey. We have set $S_0 = 4$ mJy.

The unaltered model of equation (7) is unsatisfactory at both high and low flux values. At low fluxes, the model diverges, requiring a cutoff on which the result depends. The issue of the low-flux cutoff is discussed further in § 5.6. For now, we simply impose a low-flux cutoff $S_l = 1$ mJy in the integral over S in equation (3). In addition, if the model is extended indefinitely to high fluxes, it may produce too many sources to be consistent with the lack of observed sources. This constraint nevertheless does not determine the shape of number counts above the highest flux observed. Thus, one must either implement a high-flux cutoff or assume something about the shape of the number counts beyond the region where they are measured. To address this, a single bin of the same width as the other bins has been added to the data at high fluxes, where the data are zero and the model nonzero; beyond $S_h = 7.4$ mJy, the model is zero. Fixing the upper cutoff as above and allowing the lower to float to its best-fit value produces $S_l = 1.3$ mJy. Two additional possibilities were also tried for a high-flux cutoff: (1) setting the model to zero beyond the highest filled bin resulted in a very shallow index ($\delta < 2$), and (2) allowing the highest bin to extend to infinity produced a very steep power law ($\delta > 10$). While both of these cases are unphysical, they illustrate the sensitivity of the power-law model on the high-flux cutoff. Thus, the constraints that have been adopted, while arbitrary, serve to restrict the range of possible models sufficiently to extract reasonable values of $[A,\ \delta]$. However, in light of this arbitrariness, the resulting constraint on the parameters of the power-law model must be treated with skepticism.

To fit to the model, the data are first binned. The number of sources with observed flux between s_k and s_{k+1} is denoted by n_k. We assume that the number of sources counted in any interval ds follows an approximate Poisson process and therefore that each n_k is a Poisson-distributed random variable that is independent of n_j for $k \neq j$. The same would not be true of the cumulative counts, and so the differential counts are preferred for this analysis. The likelihood of observing the data $\{n_k\}$ if the model is $\{N_k\}$ is then

$$\mathcal{L} = \prod_k \frac{N_k^{n_k}\exp(-N_k)}{n_k!}, \tag{8}$$

because it is assumed that the bins are independent. The value of the model in a given observed bin is defined as

$$N_k(\boldsymbol{p}) = \frac{1}{\Delta s}\int_{s_k}^{s_{k+1}}\left[F(s) + \int_0^{\infty} B(s,\ S)C(S)N'(S;\ \boldsymbol{p})\,dS\right]ds. \tag{9}$$

The function $-\ln\mathcal{L}$ is minimized with respect to $\boldsymbol{p}$ to find the maximum likelihood value of $\boldsymbol{p}$.

Two modifications of the likelihood equation (8) were made for this analysis. The first is that a prior was applied to constrain

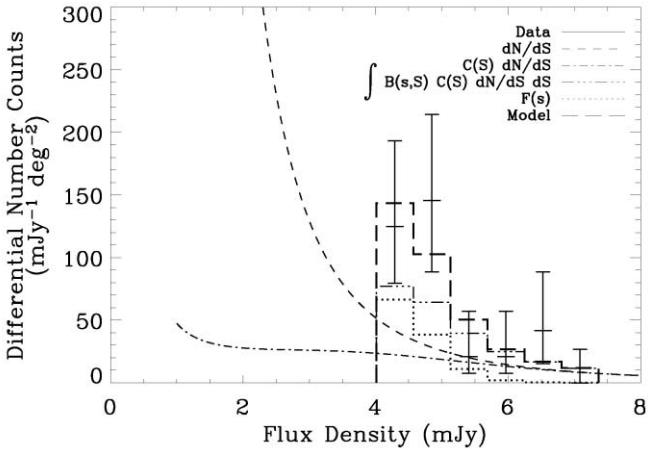

FIG. 13.—Model of the submillimeter number count distribution as a function of flux density (results of finding the maximum likelihood value of the model eq. [7]). The functions N' and $C(S)N'$ are shown as continuous functions of true flux density, S, and the data, false detection rate, $\int B(s,\ S)C(S)(N')\,dS$, and model are shown binned in the coarse bins of observed flux density, s, used for the raw data. (Note that the abscissa is used for two different flux densities, S and s.) The ordinate was scaled from the 324 arcmin^2 of the survey to 1 deg^2. The error bars on the data are Poisson errors as described in the text.

$\delta > 2$, so that both the integral of the number counts and the integral of the total flux density remained finite for $S > 0$. Thus,

$$\mathcal{L}' = \mathcal{L}\Theta(\delta - 2).$$

Second, to extract confidence regions for the fitted parameters, it was necessary to normalize $\mathcal{L}'$, such that

$$\int \mathcal{L}'(\boldsymbol{p})\,d\boldsymbol{p} = 1.$$

This normalization was done by numerical evaluation of the likelihood and its integral over the region where it is appreciably nonzero (see Fig. 14 below).

The various components of this fit are shown in Figure 13. The data are shown with 68% confidence interval error bars, based on the observed number of sources in each bin, scaled to an area of a square degree. The error bars were computed according to the prescription of Feldman & Cousins (1998) for small-number Poisson statistics (which unifies the treatment of upper confidence limits and two-sided confidence intervals). The error bar on the highest flux density bin is an upper limit. The model is clearly consistent with the data given the error bars. (All six model bins falling within the 68% confidence interval error bars of the data *may* imply that the errors have been overestimated, although this has a 10% probability of occurring.) Examining the fit in stages, one finds that the product of the survey completeness and the best-fit number counts shows that the survey incompleteness reduces the number of sources observed at low flux densities as expected; above $\sim$7 mJy, the survey is essentially complete. The effect of the bias, however, combined with the steepness of the number counts, increases the number of sources observed in all bins substantially above that of the underlying source distribution and contributes to the observed number of sources in all bins. In fact, based on the best-fit DNC and computing over the range of fluxes observed, 67% of real sources will have a true flux density *below* the detection threshold. Note that the best-fit number counts lie below the Poisson errors for the raw counts, demonstrating again that the survey bias is a nonnegligible effect. Given the

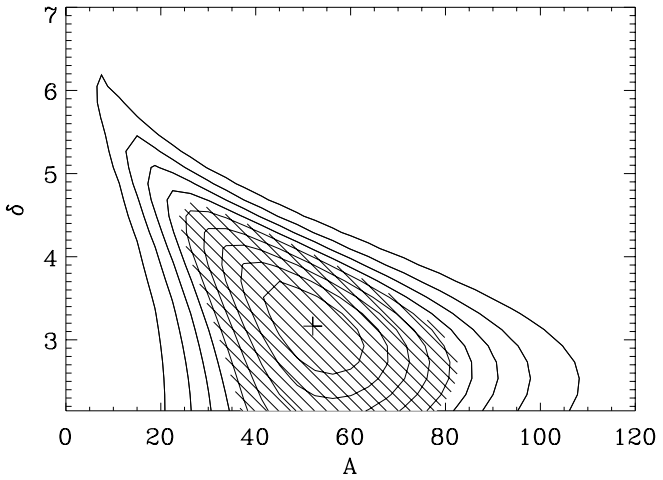

FIG. 14.—Contours of the likelihood function (eq. [8]) in the [A, δ]-plane. Contours are shown for 10%, 20%, . . . , 90% of the peak height. The location of the peak is shown by a cross, and the hatched area indicates the 68% confidence region. The maximum likelihood values are $A = 52.0$ and $\delta = 3.16$.

maximum likelihood values of A and δ (52.0 and 3.16, respectively), the cumulative source count at $S_{1.1\ \mathrm{mm}} > 2.75$ mJy is 192^{+108}_{-88} deg^{-2}. This is consistent with the 1.2 mm MAMBO number count result (378^{+136}_{-113} deg^{-2}) for the combined Lockman Hole and European Large-Area *ISO* Survey (ELAIS) N2 regions (Greve et al. 2004).

Contours of the likelihood function for this fit are shown in Figure 14. In calculating the likelihood, the upper and lower flux limits were assumed to be a correct model, and as such, the likelihood does not account for violations of this assumption. The shaded region was obtained by integrating the normalized likelihood $\mathcal{L}'$ for values $\mathcal{L}' > \mathcal{L}_{\mathrm{thresh}}$, such that the integral was equal to 0.68. These are Bayesian errors that incorporate the prior belief that $\delta > 2$.

5.6. *Difficulties and Caveats*

As the above discussion indicates, the extraction of number counts from this data set is subject to a number of difficulties and caveats. In addition to the small-number statistics and the difficulty in modeling the dependence of the survey bias and completeness on the confusion noise that have already been discussed, a separate discussion of the principal limitations of the preceding analysis is in order. These are the low S/N of the detections and the sensitivity of the result to the lowest flux objects assumed to contribute to the observed counts. These limitations may be overcome with a more sophisticated future analysis, as we discuss.

The survey bias, combined with an underlying number counts distribution rising at low fluxes, has a strong effect on the fluxes of sources observed at low S/N. This problem is exacerbated in the presence of confusion noise, but it is present in surveys in which random noise dominates over the confusion noise as well. This point has been appreciated in the historical confusion literature. Crawford et al. (1970) showed how to use a maximum likelihood method to extract a power-law slope from observed flux densities, and Murdoch et al. (1973) extended this to the case of sources observed with Gaussian noise. Because of the divergence at low fluxes of a power law, a lower limit in flux must be imposed in order to obtain finite answers. The principal conclusion of Murdoch et al. (1973) was that the power-law slope of the number counts determined by the maximum likelihood method depends sensitively on this lower cutoff if the S/N of the sources used in the survey is less than 5, whereas above this point the slope determination, while biased, is not dependent on the lower cutoff. This sensitivity to the lower flux cutoff also applies to the amplitude of the power law as well, a point that is clearly described by Marshall (1985). Although the Murdoch et al. (1973) result is for the rather unphysical case of a power law with an abrupt cutoff, the general result that derived number counts based on low-S/N sources will depend sensitively on the assumed behavior of the underlying number counts far below threshold is more general. This may be seen by considering the behavior of $C(S)N'$ as $S \rightarrow 0$. As long as this function is increasing, the bias will continue to push some sources of low intrinsic flux up above the detection threshold, and so the low-S/N regime will contain sources from well below threshold. [Note that this is consistent with the behavior of $B(s, S)$, since for s greater than threshold, B is positive for all values of S.] One can see from Figure 11 that the completeness drops off rather slowly for Gaussian noise (and even more slowly when confusion noise is added) and never vanishes. In fact, the product of the Gaussian completeness times any $S^{-\delta}$, $\delta > 0$, diverges as $S \rightarrow 0$, so for many otherwise reasonable number counts models, this problem will occur. Thus, in the presence of any sort of bias, whether due to confusion or noise, deriving accurate counts above threshold requires a nontrivial amount of information about the counts well below threshold if the S/N of the detections is low. Since all of our sources have S/N ≤ 5, any constraint placed on the power-law amplitude and slope will likely depend sensitively on the lower cutoff chosen.

An analysis technique that overcomes all of the shortcomings mentioned above is the so-called fluctuation or "$P(D)$" analysis (Scheuer 1957, 1974; Condon 1974). This analysis matches the shape of the observed pixel value distribution (Fig. 6) against the prediction for a model distribution combined with the instrument noise. It overcomes the small-number statistics by using the full map instead of only the above-threshold detections. It addresses the nonlinear aspects of equation (3) by directly including the confusion noise. Low S/N is no longer an issue, since individual sources are no longer considered, and the lowest flux considered is naturally at the confusion limit where additional sources contribute only a mean to the observed histogram. The unchopped scan strategy of the Lockman Hole data simplifies such an analysis because of the simplicity of the effective beam. Additional effects such as the attenuation of large angular scale structure by the atmospheric cleaning or the angular correlation of sources may also be straightforwardly included. A paper on this analysis is in preparation.

6. DISCUSSION

6.1. *Comparison with Previous Number Count Results*

A number of other groups have previously published number counts of submillimeter galaxies. Figure 15 shows selected recent results. These include surveys of blank fields by SCUBA on the JCMT at 850 μm (Barger et al. 1999; Borys et al. 2003; Scott et al. 2002), observations of galaxies lensed by clusters, also using SCUBA at 850 μm (Blain et al. 1999; Chapman et al. 2002; Cowie et al. 2002; Smail et al. 2002), and blank-field surveys by MAMBO on the IRAM telescope (Greve et al. 2004). The Bolocam result is plotted as the maximum likelihood cumulative number counts (computed from the DNC described in § 5.5), evaluated from 1 mJy to the maximum observed flux density (6.8 mJy). The number counts in the figure are not adjusted for the wavelength differences of the surveys.

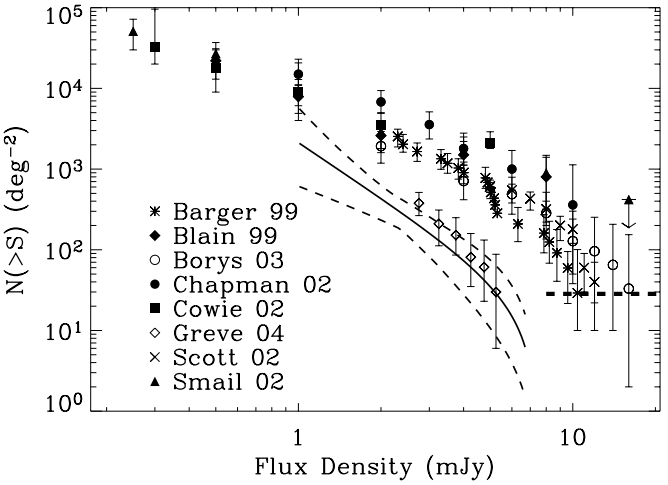

FIG. 15.—Previous measurements of the number counts of submillimeter galaxies, along with the new measurement with Bolocam. Previous surveys that used lensing by clusters are indicated by filled symbols; all other symbols indicate blank-field surveys. The solid line shows the integral of the Bolocam maximum likelihood differential number counts; the region between the dashed curves is the 68% confidence region of Fig. 14 translated into the range of possible cumulative number counts. The thick horizontal dashed line is the 90% upper confidence limit for sources brighter than 8 mJy for this survey. All surveys are at 850 μm, except for Bolocam at 1100 μm and Greve et al. (2004) (IRAM MAMBO) at 1200 μm. See §§ 5.5 and 5.6 for a description of the limitations of this model.

The Bolocam result is in broad agreement with previous measurements; the maximum likelihood cumulative number counts are consistent with the 1200 μm measurement and below the 850 μm measurements, as expected if the same population of objects is being measured. The region of 68% probability in parameter space has been translated to cumulative number counts and is shown by the region between the dashed curves. This region does not correspond to the naive expectation of Poisson errors based on the number of detected sources. This is due to both the strong effect of the bias and the flux cutoffs imposed on the model. Because of the bias, it is inappropriate to assume that the number of observed sources in a bin can be used as a measure of the uncertainty in the underlying number counts in that bin. The effect of assuming an upper flux cutoff is particularly evident in the figure in the rapid drop of the cumulative counts as the cutoff is approached. This causes the error bars to be artificially small, as any model is constrained to be zero beyond this point. The maximum likelihood number count model presented here, as well as its errors, depends strongly on the exact low- and high-flux cutoffs assumed for the underlying distribution and consequently cannot be treated as definitive.

In addition to the caveats above, it should be borne in mind that the uncertainty of the flux bias discussed in § 3.4 (derived from the rms pointing error between the Bolocam galaxy candidates and coincident radio sources) introduces a systematic shift in the simple model of equation (7): the parameter A changes by an amount $(1 \pm \sigma_\epsilon/\epsilon)^{-\delta}$. This gives a steep dependence of the amplitude of the number counts on the calibration error and the presumed power-law index.

At high flux densities, where the survey is nearly complete and the effect of the bias is smallest, model-independent constraints may be obtained. In particular, the lack of any observed sources with flux density greater than 8 mJy has been used to place a 90% upper confidence limit on the cumulative number counts above 8 mJy; this is shown by the dashed horizontal line in the figure. This constraint depends only linearly on the calibration error. Bolocam appears to be measuring near the region where the number counts, based on both the 850 and 1200 μm measurements, would be expected to turn over, but because of the limited survey area, we do not strongly constrain the number counts at the bright end of the luminosity function.

6.2. *Integrated Flux Density*

The fraction of the FIRAS integrated far-infrared background light (Fixsen et al. 1998) measured by this survey can be computed in several ways. Summing the flux densities of all observed sources gives 85 mJy, or 3.9% of the FIRAS background over the survey area at 1.1 mm (8.0×10^{-22} W m^{-2} sr^{-1} Hz^{-1}). Subtracting out the expected mean flux of false detections gives 58 mJy, or 2.7% of the FIRAS background. Integrating the maximum likelihood DNC between 1 and 6.8 mJy (the maximum observed) gives 276 mJy, or ~13% of the FIRAS background. Since it seems plausible that the number counts do in fact steepen beyond the upper range of our observations, we conclude that at least ~95% of the light from submillimeter sources lies below the detection threshold of this survey and ~87% below the minimum flux derived from our number counts model.

6.3. *Implied Luminosities and Star Formation Rates*

The flux density of a galaxy at an observed frequency, ν, is related to its intrinsic luminosity, L, by (Blain et al. 2002)

$$S_\nu = \frac{1+z}{4\pi D_L^2} L \frac{f_{\nu(1+z)}}{\int f_{\nu'}\, d\nu'}, \tag{10}$$

where D_L is the luminosity distance to redshift z, $f_{\nu(1+z)}$ is the redshifted SED of the galaxy, and $\int f_{\nu'}\, d\nu'$ is the integrated rest SED. For a flat ($\Omega_k = 0$) cosmology, it can be shown (e.g., Peebles 1993) that the luminosity distance is given by

$$D_L = \frac{c(1+z)}{H_0} \int_0^z \frac{1}{\Omega_M (1+z')^3 + \Omega_\Lambda}\, dz'.$$

To estimate the bolometric luminosities of the submillimeter galaxies detected by Bolocam, a template SED was constructed that assumes a blackbody emission spectrum modified by a dust emissivity term:

$$f_\nu \propto \epsilon_\nu B_\nu(T) \propto [1 - \exp(-\tau_\nu)] B_\nu(T), \tag{11}$$

where $B_\nu(T)$ is the Planck function evaluated at dust temperature, T, and frequency, ν, and τ_ν is the optical depth of the dust:

$$\tau_\nu = \left(\frac{\nu}{\nu_0}\right)^\beta.$$

The dust emissivity index, β, is believed to lie between 1 and 2 (Dunne et al. 2000). The form of equation (11) is commonly assumed in the literature for dusty nearby galaxies and high-redshift AGNs, including Benford et al. (1999), Omont et al. (2001), Priddey & McMahon (2001), and Isaak et al. (2002). This equation reduces to a simple optically thin emission spectrum, $\epsilon_\nu B_\nu(T) \sim \nu^{2+\beta}$, in the Rayleigh-Jeans limit and $\nu \ll \nu_0$, and it asymptotes to $B_\nu(T)$ at high frequencies (because

an emissivity of >1 is unphysical). Observations of luminous low-redshift galaxies (Arp 220 and Mrk 231) and high-redshift galaxies detected by deep submillimeter surveys furthermore suggest that a power law, $f_\nu \propto \nu^\alpha$, is appropriate to model the hotter components of dust on the Wien side of the spectrum (Blain et al. 1999). We implement such a power law at high frequencies, matched to equation (11) at $1.2\nu_0$.

Creating a composite SED of nearby dusty *IRAS* galaxies, high-redshift submillimeter galaxies, gravitationally lensed high-redshift galaxies, and high-redshift AGNs (Blain et al. 2002 and references therein), we find that parameters of $T = 40$ K, $\nu_0 = 3700$ GHz, $\beta = 1.6$, and $\alpha = -1.7$ provide a reasonable fit. Assuming a cosmology of $\Omega_\lambda = 0.7$, $\Omega_M = 0.3$, and $h_0 = 0.73$ and a galaxy redshift of $z = 2.4$ (the median redshift that Chapman et al. [2003b] derive for their sample of 10 submillimeter galaxies identified using high-resolution radio observations), equation (10) gives extreme bolometric luminosities of $L = (1.0-1.6) \times 10^{13}\ L_\odot$ for the range of flux densities detected by Bolocam. The derived luminosities are insensitive to redshift, varying by less than 25% for $0.6 < z < 12$. Assuming dust temperatures of 30 and 50 K implies luminosities of $(3.5-5.9) \times 10^{12}$ and $(1.8-3.0) \times 10^{13}\ L_\odot$, respectively. If these galaxies are lensed, their intrinsic luminosities will be lower.

Observations of nearby star-forming galaxies suggest the following relation between the SFR present in a galaxy and its far-infrared luminosity:

$$\mathrm{SFR} = \epsilon \times 10^{-10}\, \frac{L_{60\,\mu\mathrm{m}}}{L_\odot}\ M_\odot\ \mathrm{yr}^{-1},$$

where $L_{60\,\mu\mathrm{m}}$ is the 60 μm luminosity. The value of ϵ varies in the literature from 2.1 to 6.5 (Scoville & Young 1983; Thronson & Telesco 1986; Rowan-Robinson et al. 1997) because of different assumptions about the duration of the starburst, different initial mass functions (IMFs), and lower mass limits. In this paper we adopt a value of $\epsilon = 2.1$ from a "cirrus" model that combines very small grains and polycyclic aromatic hydrocarbons (PAHs) with a Salpeter IMF in a starburst of OBA stars over 2×10^6 yr (Thronson & Telesco 1986). Obtaining $L_{60\,\mu\mathrm{m}}$ from our model SED yields large SFRs of 480–810 $M_\odot$ yr^{-1}. While these calculated luminosities and SFRs are sensitive to the SED model parameters, particularly T and β, most recent models of local star-forming galaxies nevertheless result in dust temperatures and emissivities that imply extreme luminosities and SFRs. It is possible, however, that these extremely luminous galaxies derive some of their power from AGNs (e.g., Alexander et al. 2003), in which case the SFRs have been overestimated. Observations of ultraluminous infrared galaxies (ULIRGs) in the local universe ($z \lesssim 0.1$) with luminosities $>10^{13}\ L_\odot$ show that nearly all of these galaxies possess luminous AGNs and that the dominant power source in the majority of nearby ULIRGs may be AGNs rather than star formation (Sanders 1999). Recent X-ray observations and optical spectroscopic data of $z > 1$ ultraluminous galaxies, however, indicate that in almost all cases the AGNs account for <20% of the total bolometric output of higher redshift galaxies (Alexander et al. 2004). *Spitzer* observations will prove useful in investigating the incidence of AGNs versus star formation in submillimeter galaxies from the shape of the mid-infrared continuum emission; initial results confirm the high-redshift X-ray results and show a mixture of infrared-warm AGNs and cooler starburst-dominated sources (Egami et al. 2004; Frayer et al. 2004), with a smaller fraction (~25%) of energetically important AGNs (Ivison et al. 2004).

7. FUTURE WORK

Observations at shorter submillimeter wavelengths are vital to both confirm the Bolocam galaxy candidate detections and make photometric redshift and temperature estimates. Follow-up 350 μm photometry of the Bolocam-detected submillimeter galaxies with SHARC-II is planned to fill in the SEDs of these galaxies. Precise astrometry afforded by the radio identifications (as well as the 10″ beam size of SHARC-II) will allow optical and infrared counterparts to be identified. Furthermore, *Spitzer* far-infrared observations combined with the Bolocam 1.1 mm galaxy survey will provide a flux density ratio that is strongly dependent on redshift for a given temperature. This is because the rest wavelength corresponding to the observed *Spitzer* wavelength of 70 μm is on the rapidly falling Wien side of the graybody spectrum (for a $z \sim 2$ galaxy at 40 K), and Bolocam's 1.1 mm observations are on the steep $\nu^{2+\beta}$ ($\beta \approx 1.5$) modified Rayleigh-Jeans side of the SED. The ratio of $S_{1.1\ \mathrm{mm}}/S_{70\ \mu\mathrm{m}}$ is thus highly dependent on redshift, growing by a factor of 250 from $z = 1$ to 5. *Spitzer* IRAC observations will also provide independent photometric redshift determinations from the SEDs of stellar populations of submillimeter galaxies redshifted into the near-IR. These combined observations, in conjunction with the radio–to–far-infrared correlation (Yun & Carilli 2002), will thus allow the temperature and redshift distributions of these submillimeter galaxies to be constrained. A detailed discussion of the SEDs and photometric redshift/temperature estimates of the Lockman Hole galaxies will follow in a companion paper (in preparation).

As discussed in § 6.1, this survey does not constrain the number counts at flux densities above 7 mJy, at approximately the break point where the number counts are expected to drop sharply (based on the 850 μm observations in Fig. 15). This can be addressed with a survey covering a larger area to shallower depth. Such a survey has been started with Bolocam in the COSMOS field,[11] which currently covers ~1000 arcmin^2. This survey should allow either determination or a strong upper limit on the 1.1 mm number counts beyond 7 mJy, as well as uncover extremely bright, interesting sources, perhaps with strong AGN components that should be easy to follow up at other wavelengths. In addition to the wide area, the COSMOS observations have extremely uniform coverage (<3% rms) and a highly cross linked scan strategy that aids in rejecting atmospheric $1/f$ noise better than the Lockman Hole observations.

8. CONCLUSIONS

Bolocam is a new bolometer camera with a large field of view and a rapid mapping speed optimized for surveys, including surveys for rare, bright submillimeter galaxies. We have used Bolocam on the Caltech Submillimeter Observatory at a wavelength of 1.1 mm to conduct a survey of 324 arcmin^2 toward the Lockman Hole for submillimeter galaxies. Unlike previous submillimeter surveys, the observations were made without chopping, at a fast scan rate of 60″ s^{-1}. The Bolocam survey encompasses the entire 850 μm 8 mJy JCMT SCUBA and 1.2 mm IRAM MAMBO surveys to a comparable depth under the assumption of a model SED for a galaxy at $z = 2.4$, with relative rms of $1 : 0.9 : 0.6–1.4$, respectively. We have reduced the resulting data set using a custom IDL-based software pipeline, in which correlated atmospheric and instrument noise is rigorously removed via a PCA sky subtraction technique. We detect 17 galaxies at a significance of $\geq 3\ \sigma$, where the map rms is ~1.4 mJy.

[11] See http://www.astro.caltech.edu/cosmos.

A series of simulations have allowed us to verify the robustness of the galaxy candidates. Extensive jackknife and pointing jitter tests reveal that the sources detected in this survey have a small characteristic length scale (point sources) and are contributed to by the ensemble of observations, strongly indicating that the galaxy candidates are real. Simulations of the observations using both synthetic maps and observational data indicate that six false detections should be expected.

Comparing our detections to those of other surveys (including SCUBA 850 μm, MAMBO 1.2 mm, and VLA radio observations) indicates that the majority of Bolocam sources have coincident detections in at least two other wavebands; we conclude that a majority of the Bolocam detections are real. Six of the detections are galaxies previously detected by the SCUBA 8 mJy survey. Of the remaining 11 Bolocam detections, 9 of them lie outside the SCUBA survey region, and we cannot search for counterparts for them. Seven of the 17 Bolocam detections have been detected by the MAMBO 1.2 mm survey, with 6 of the remaining 10 sources lying outside the MAMBO good coverage region. While both the SCUBA and MAMBO surveys detect most of the Bolocam sources in the overlap region, neither Bolocam nor SCUBA/MAMBO detect the majority of the remaining SCUBA and MAMBO sources. A total of 65% of the 17 Bolocam source candidates have at least one radio coincidence, although the accidental radio detection rate is high (34%) owing to the size (31″ FWHM) of the Bolocam beam. Furthermore, we statistically detect the aggregate average of the SCUBA and MAMBO sources below our 3 σ detection threshold at significances of 3.3 and 4.0 σ, respectively.

Further simulations enabled us to estimate the completeness and bias of this survey, which were subsequently used with the false detection rate to fit a simple power-law model of the underlying parent distribution to match the observed number count distribution. This model constrains the submillimeter counts over the flux density range $S_{1.1\,\mathrm{mm}} = 1-7$ mJy. While the validity of this model is significantly limited by both the effects of confusion noise and the flux density cutoffs assumed for the underlying number count distribution, we find this modeled number count distribution to be consistent with previously published submillimeter galaxy number counts. Integrating the maximum likelihood differential number counts distribution between 1 and 6.8 mJy (the maximum observed flux density) yields 276 mJy in the map, or $\sim$13% of the FIRAS integrated far-infrared background light.

If the Bolocam galaxy candidates lie at redshifts $z > 1$, then their inferred luminosities are $L = (1.0-1.6) \times 10^{13}\ L_{\odot}$ (assuming a dust temperature of 40 K). Further assuming that they are powered by star formation, large SFRs of 480–810 $M_{\odot}$ yr^{-1} are implied. Multiwavelength follow-up observations of the Lockman Hole field are underway with *Spitzer* and SHARC-II in order to constrain the temperature/redshift distributions of these sources.

With alacrity, we acknowledge the support of the CSO director and staff, the support of Kathy Deniston, and helpful conversations with Andrew Blain, Steven Eales, and Min Yun. This work was supported in part by NSF grants AST 00-98737, AST 99-80846, and AST 02-06158 and PPARC grants PPA/Y/S/2000/00101 and PPA/G/O/2002/00015. D. H. acknowledges the support of a PPARC Ph.D. Fellowship, S. R. G. acknowledges Caltech for the R. A. Millikan Fellowship, and G. T. L. acknowledges NASA for GSRP Fellowship NGT5-50384.

REFERENCES

Alexander, D. M., Bauer, F. E., Chapman, S. C., Smail, I., Blain, A. W., Brandt, W. N., & Ivison, R. J. 2004, preprint (astro-ph/0401129)
Alexander, D. M., et al. 2003, AJ, 125, 383
Almaini, O., et al. 2003, MNRAS, 338, 303
Aretxaga, I., Hughes, D. H., Chapin, E. L., Gaztanaga, E., Dunlop, J. S., & Ivison, R. J. 2003, MNRAS, 342, 759
Barger, A. J., Cowie, L. L., & Sanders, D. B. 1999, ApJ, 518, L5
Benford, D. J., Cox, P., Omont, A., Phillips, T. G., & McMahon, R. G. 1999, ApJ, 518, L65
Bertoldi, F., et al. 2000, A&A, 360, 92
Blain, A. W., Chapman, S. C., Smail, I., & Ivison, R. 2004, ApJ, 611, 725
Blain, A. W., Kneib, J.-P., Ivison, R. J., & Smail, I. 1999, ApJ, 512, L87
Blain, A. W., Smail, I., Ivison, R. J., Kneib, J.-P., & Frayer, D. T. 2002, Phys. Rep., 369, 111
Borys, C., Chapman, S., Halpern, M., & Scott, D. 2003, MNRAS, 344, 385
Carilli, C. L., & Yun, M. S. 1999, ApJ, 513, L13
Chapman, S. C., Blain, A., Ivison, R., & Smail, I. 2003a, in ASP Conf. Ser. 297, Star Formation through Time, ed. E. Perez, R. M. Gonzalez Delgado, & G. Tenorio-Tagle (San Francisco: ASP), 289
———. 2003b, Nature, 422, 695
Chapman, S. C., Blain, A. W., Smail, I., & Ivison, R. J. 2005, ApJ, 622, 772
Chapman, S. C., Scott, D., Borys, C., & Fahlman, G. G. 2002, MNRAS, 330, 92
Ciliegi, P., Zamorani, G., Hasinger, G., Lehmann, I., Szokoly, G., & Wilson, G. 2003, A&A, 398, 901
Condon, J. J. 1974, ApJ, 188, 279
Cowie, L. L., Barger, A. J., & Kneib, J.-P. 2002, AJ, 123, 2197
Crawford, D. F., Jauncey, D. L., & Murdoch, H. S. 1970, ApJ, 162, 405
Dunne, L., Eales, S., Edmunds, M., Ivison, R., Alexander, P., & Clements, D. L. 2000, MNRAS, 315, 115
Eales, S., Bertoldi, F., Ivison, R., Carilli, C., Dunne, L., & Owen, F. 2003, MNRAS, 344, 169
Eddington, A. S. 1913, MNRAS, 73, 359
———. 1940, MNRAS, 100, 354
Egami, E., et al. 2004, ApJS, 154, 130
Feldman, G. J., & Cousins, R. D. 1998, Phys. Rev. D, 57, 3873
Fixsen, D. J., Dwek, E., Mather, J. C., Bennett, C. L., & Shafer, R. A. 1998, ApJ, 508, 123
Fox, M. J., et al. 2002, MNRAS, 331, 839
Frayer, D. T., Ivison, R. J., Scoville, N. Z., Yun, M., Evans, A. S., Smail, I., Blain, A. W., & Kneib, J.-P. 1998, ApJ, 506, L7
Frayer, D. T., et al. 1999, ApJ, 514, L13
———. 2004, ApJS, 154, 137
Glenn, J., et al. 1998, Proc. SPIE, 3357, 326
———. 2002, Appl. Opt., 41, 136
———. 2003, Proc. SPIE, 4855, 30
Greve, T. R., Ivison, R. J., Bertoldi, F., Stevens, J. A., Dunlop, J. S., Lutz, D., & Carilli, C. L. 2004, MNRAS, 354, 779
Haig, D. J., et al. 2004, Proc. SPIE, 5498, 78
Hasinger, G., et al. 2001, A&A, 365, L45
Hauser, M. G., et al. 1998, ApJ, 508, 25
Holland, W. S., et al. 1999, MNRAS, 303, 659
Isaak, K. G., Priddey, R. S., McMahon, R. G., Omont, A., Peroux, C., Sharp, R. G., & Withington, S. 2002, MNRAS, 329, 149
Ivison, R. J., et al. 2002, MNRAS, 337, 1
———. 2004, ApJS, 154, 124
Jahoda, K., Lockman, F. J., & McCammon, D. 1990, ApJ, 354, 184
Jenness, T., Stevens, J. A., Archibald, E. N., Economou, F., Jessop, N. E., & Robson, E. I. 2002, MNRAS, 336, 14
Marshall, H. L. 1985, ApJ, 289, 457
Murdoch, H. S., Crawford, D. F., & Jauncey, D. L. 1973, ApJ, 183, 1
Murtagh, F., & Heck, A. 1987, Multivariate Data Analysis (Dordrecht: Reidel)
Neri, R., et al. 2003, ApJ, 597, L113
Omont, A., Cox, P., Bertoldi, F., McMahon, R. G., Carilli, C., & Isaak, K. G. 2001, A&A, 374, 371
Peebles, P. J. E. 1993, Principles of Physical Cosmology (Princeton: Princeton Univ. Press)
Priddey, R. S., & McMahon, R. G. 2001, MNRAS, 324, L17
Puget, J.-L., Abergel, A., Bernard, J.-P., Boulanger, F., Burton, W. B., Desert, F.-X., & Hartmann, D. 1996, A&A, 308, L5
Rodighiero, G., & Franceschini, A. 2004, A&A, 419, L55
Rowan-Robinson, M., et al. 1997, MNRAS, 289, 490

Sandell, G. 1994, MNRAS, 271, 75
Sanders, D. B. 1999, Ap&SS, 266, 331
Scheuer, P. A. G. 1957, Proc. Cambridge Philos. Soc., 53, 764
———. 1974, MNRAS, 166, 329
Scott, S. E., et al. 2002, MNRAS, 331, 817
Scoville, N. Z., & Young, J. S. 1983, ApJ, 265, 148
Sheth, K., Blain, A. W., Kneib, J., Frayer, D. T., van der Werf, P. P., & Knudsen, K. K. 2004, ApJ, 614, L5
Smail, I., Ivison, R. J., Blain, A. W., & Kneib, J.-P. 2002, MNRAS, 331, 495
Swinbank, A. M., Smail, I., Chapman, S. C., Blain, A. W., Ivison, R. J., & Keel, W. C. 2004, ApJ, 617, 64
Thronson, H., & Telesco, C. 1986, ApJ, 311, 98
Yun, M. S., & Carilli, C. L. 2002, ApJ, 568, 88